Astronomy & Astrophysics manuscript no. output
October 27, 2020

Six transiting planets and a chain of Laplace resonances in TOI-178

A. Leleu[⋆1,2], Y. Alibert[2], N. C. Hara[⋆1], M. J. Hooton[2], T. G. Wilson[3], P. Robutel[4], J.-B. Delisle[1], J. Laskar[4], S. Hoyer[5], C. Lovis[1], E. M. Bryant[6,7], E. Ducrot[8], J. Cabrera[9], J. Acton[10], V. Adibekyan[11,12,13], R. Allart[1], C. Allende Prieto[14,15], R. Alonso[14,15], D. Alves[16], D. R. Anderson[6,7], D. Angerhausen[17], G. Anglada Escudé[18,19], J. Asquier[20], D. Barrado[21], S. C. C. Barros[11,13], W. Baumjohann[22], D. Bayliss[6,7], M. Beck[1], T. Beck[2], A. Bekkelien[1], W. Benz[2,23], N. Billot[1], A. Bonfanti[22], X. Bonfils[24], F. Bouchy[1], V. Bourrier[1], G. Boué[4], A. Brandeker[25], C. Broeg[2], M. Buder[26], A. Burdanov[8,27], M. R. Burleigh[10], T. Bárczy[28], A. C. Cameron[3], S. Chamberlain[10], S. Charnoz[29], B. F. Cooke[6,7], C. Corral Van Damme[20], A. C. M. Correia[30,4], S. Cristiani[31], M. Damasso[32], M. B. Davies[33], M. Deleuil[5], L. Delrez[34,35,1], O. D. S. Demangeon[11,13], B.-O. Demory[23], P. Di Marcantonio[31], G. Di Persio[36], X. Dumusque[1], D. Ehrenreich[1], A. Erikson[9], P. Figueira[11,37], A. Fortier[2,23], L. Fossati[22], M. Fridlund[38,39], D. Futyan[1], D. Gandolfi[40], A. García Muñoz[41], L. Garcia[8], S. Gill[6,7], E. Gillen[⋆⋆42,43], M. Gillon[34], M. R. Goad[10], J.I. González Hernández[14,15], M. Guedel[44], M. N. Günther[⋆⋆⋆45], J. Haldemann[2], B. Henderson[10], K. Heng[23], A. E. Hogan[10], E. Jehin[46], J. S. Jenkins[47,48], A. Jordán[49,50], L. Kiss[51], M. H. Kristiansen[52,53], K. Lam[9], B. Lavie[1], A. Lecavelier des Etangs[54], M. Lendl[1], J. Lillo-Box[21], G. Lo Curto[37], D. Magrin[55], C. J. A. P. Martins[11,12], P. F. L. Maxted[56], J. McCormac[57], A. Mehner[37], G. Micela[58], P. Molaro[31,59], M. Moyano[60], C. A. Murray[43], V. Nascimbeni[55], N. J. Nunes[61], G. Olofsson[25], H. P. Osborn[23,45], M. Oshagh[14,15], R. Ottensamer[62], I. Pagano[63], E. Pallé[64,65], P. P. Pedersen[43], F. A. Pepe[1], C.M. Persson[39], G. Peter[26], G. Piotto[55,66], G. Polenta[67], D. Pollacco[68], E. Poretti[69,70], F. J. Pozuelos[34,35], F. Pozuelos[8,46], D. Queloz[1,43], R. Ragazzoni[55], N. Rando[20], F. Ratti[20], H. Rauer[9,41,71], L. Raynard[10], R. Rebolo[14,15], C. Reimers[62], I. Ribas[18,19], N. C. Santos[11,13], G. Scandariato[63], J. Schneider[72], D. Sebastian[73], M. Sestovic[23], A. E. Simon[2], A. M. S. Smith[9], S. G. Sousa[11], A. Sozzetti[32], M. Steller[22], A. Suárez Mascareño[14,15], G. M. Szabó[74,75], D. Ségransan[1], N. Thomas[2], S. Thompson[43], R. H. Tilbrook[10], A. Triaud[73], S. Udry[1], V. Van Grootel[35], H. Venus[26], F. Verrecchia[67,76], J. I. Vines[16], N. A. Walton[77], R. G. West[6,7], P. J. Wheatley[6,7], D. Wolter[9], and M. R. Zapatero Osorio[78]

(Affiliations can be found after the references)

October 27, 2020

ABSTRACT

Determining the architecture of multi-planetary systems is one of the cornerstones of understanding planet formation and evolution. Among these, resonant systems are especially important as the fragility of their orbital configuration ensure that no significant scattering or collisional event took place since the earliest formation phase, when the parent protoplanetary disk was still present. In this context, TOI-178 has been the subject of particular attention as the first *TESS* observations hinted at the possible presence of a near 2:3:3 resonant chain. Here we report the results of observations from *CHEOPS*, ESPRESSO, NGTS, and SPECULOOS with the aim of deciphering the peculiar orbital architecture of the system. We show that TOI-178 harbours at least six planets in the super-Earth to mini-Neptune regimes with radii ranging from 1.177 ± 0.074 to 2.91 ± 0.11 Earth radii, and periods of 1.91, 3.24, 6.56, 9.96, 15.23, and 20.71 d. All planets but the innermost one form a 2:4:6:9:12 chain of Laplace resonances, and the planetary densities show important variations from planet to planet, jumping from $0.90^{+0.16}_{-0.21}$ to $0.15^{+0.03}_{-0.04}$ times the Earth density between planets *c* and *d*. Using Bayesian interior structure retrieval models, we show that the amount of gas in the planets does not vary in a monotoneous way as one could expect from simple formation and evolution models, contrarily to other known systems in chain of Laplace resonances. The brightness of TOI-178 (H=8.76 mag, J=9.37 mag, V=11.95 mag) allows for precise characterisation of its orbital architecture as well as of the physical nature of the six presently known transiting planets it harbours. The peculiar orbital configuration and the diversity in average density among the planets in the system will enable the study of planetary interior structures and atmospheric evolution providing important clues on the formation of super-Earths and mini-Neptunes.

Key words. see on AA website. Transits · Mean-motion resonance · Laplace resonance · CHEOPS · TESS · NGTS · SPECULOOS

1. Introduction

Since the discovery of the first exoplanet orbiting a Sun-like star by Mayor & Queloz (1995), the diversity of observed planetary systems has continued to challenge our understanding of their formation and evolution. As an ongoing effort to understand these physical processes, observational facilities strive to get the full picture of exoplanetary systems by looking for additional candidates to known systems, along with better constraining the orbital architecture, radii and masses of the known planets.

In particular, chains of planets in mean-motion resonances (MMRs) are 'Rosetta Stones' of the formation and evolution of planetary systems. Indeed, our current understanding of planetary system formation theory implies that such configurations are a common outcome of protoplanetary discs: slow convergent migration of a pair of planets in quasi-circular orbits leads to a high probability of capture in first order MMRs - the period ratio of the two planets is equal to $(k+1)/k$, with k an integer (Lee & Peale 2002; Correia et al. 2018). As the disc strongly damps the eccentricities of the protoplanets, this mechanism can repeat itself, trapping the planets in a chain of MMRs, leading to very closely packed configurations (Lissauer et al. 2011). However, resonant configurations are not most common orbital arrangements (Fabrycky et al. 2014). As the protoplanetary disc dissipates, the eccentricity damping lessens, which can lead to instabilities in packed systems (see for example Terquem & Papaloizou 2007; Pu & Wu 2015; Izidoro et al. 2017).

For planets that remained in resonance, and are close enough to their host star, tides become the dominant force that affect the architecture of the systems, which can then lead to a departure of the period ratio from the exact resonance (Henrard & Lemaitre 1983; Papaloizou & Terquem 2010; Delisle et al. 2012). In some near-resonant systems, such as HD 158259, the tides seem to have pulled the configuration entirely out of resonance (Hara et al. 2020). However, through gentle tidal evolution it is possible to retain a resonant state even with null eccentricities, through three-body resonances (Morbidelli 2002; Papaloizou 2015). Such systems are too fine-tuned to result from scattering events, and hence can be used to constrain the outcome of protoplanetary discs (Mills et al. 2016).

A Laplace resonance, in reference to the configuration of Io, Europa, and Ganymede, is a three body resonance where each consecutive pair of bodies are in, or close to, two planet MMRs. To date, very few systems were observed in a chain of Laplace resonances : Kepler-60 (Goździewski et al. 2016), Kepler-80 (MacDonald et al. 2016), Kepler-223 (Mills et al. 2016), and Trappist-1 (Gillon et al. 2017; Luger et al. 2017). No radial velocity follow-up has been made for these system so far, mainly due to the relative faintness of their host star in the visible (V magnitudes greater than ∼14). However, TTVs could be used to estimate the mass of their planets, see for example Agol et al. (2020) for the case of Trappist-1.

In this study, we present photometric and RV observations of TOI-178, a V = 11.95 mag, K-type star, first observed by *TESS* in its sector 2. We jointly analyse the photometric data of *TESS*, two nights of NGTS and SPECULOOS data, and 285 hours of *CHEOPS* observations, along with forty-six ESPRESSO radial velocity points. This follow-up effort allows us to decipher the architecture of the system and demonstrate the presence of a chain of Laplace resonances between the five outer planets.

We begin in section 2 by presenting the rationale that led to the *CHEOPS* observation sequence (two visits totaling 11 d followed by two shorter visits). In section 3 we describe the parameters of the star. In section 4, we present the photometric and RV data we use in the paper. In section 5, we show how these data led us to the detection of 6 planets, the five outer one being in a chain of Laplace resonances, and to constrain their parameters. In section 6, we explain the resonant state of the system and discuss its stability. In section 6.4, we describe the transit timing variations (TTVs) that this system could potentially exhibit in the coming years. Conclusions are presented in section 8.

2. CHEOPS observation strategy

CHEOPS observation consisted in one long double visit (11 days) followed by to short visits (a few hours each) at precise dates. We explain in this section how we came up to this particular observation strategy. Details on all data used and acquired, as well as on their analysis, are presented in the following sections.

The first release of candidates from the *TESS* alerts of Sector 2 included three planet candidates in TOI-178 with periods of 6.55 d, 10.35 d, and 9.96 d, respectively. Based on these data, TOI-178 was identified as a potential co-orbital system (Leleu et al. 2019) with two planets oscillating around the same period. This prompted ESPRESSO RV measurements and two sequences of simultaneous ground-based photometric observations with NGTS and SPECULOOS. From the latter, no transit was observed for TOI-178.02 ($P = 10.35$ d) in September 2019, however a transit ascribed to this candidate was detected one month later by NGTS and SPECULOOS. The absence of transit of TOI-178.02 noted above, combined with the three transits observed by *TESS* at high SNR (above 10), was interpreted as an additional sign of the strong TTVs expected in a co-orbital configuration. This solution was supported by RV data that were consistent with horseshoe orbits of similar mass objects (Leleu et al. 2015).

A continuous 11 d *CHEOPS* observation (split in two visits for scheduling reasons) was therefore performed in August 2020 in order to confirm the orbital configuration of the system, as the instantaneous period of both members of the co-orbital pair would always be smaller than 11 d, and thus at least one transit of both targets should be detectable. Analysis of this light curve led to the confirmation of the presence of two of the planets already discovered by *TESS* (in this study denoted as planets d and e with periods of 6.55 d and 9.96 d, respectively) and the detection of two new inner transiting planets (denoted planets b and c, respectively with periods of 1.9 d and 3.2 d). However, one of the planets belonging to the proposed co-orbital pair (period of 10.35 d) was not apparent in the light curve. A potential hypothesis was that the first and third transit of the TOI-178.02 candidate ($P = 10.35$ d) during *TESS* Sector 2 belonged to a planet of twice the period (20.7 d), while the second transit would belong to another planet of unknown period. This scenario was supported by the two ground-based observations mentioned above, as a

⋆ CHEOPS Fellow
⋆⋆ Winton Fellow
⋆⋆⋆ Juan Carlos Torres Fellow

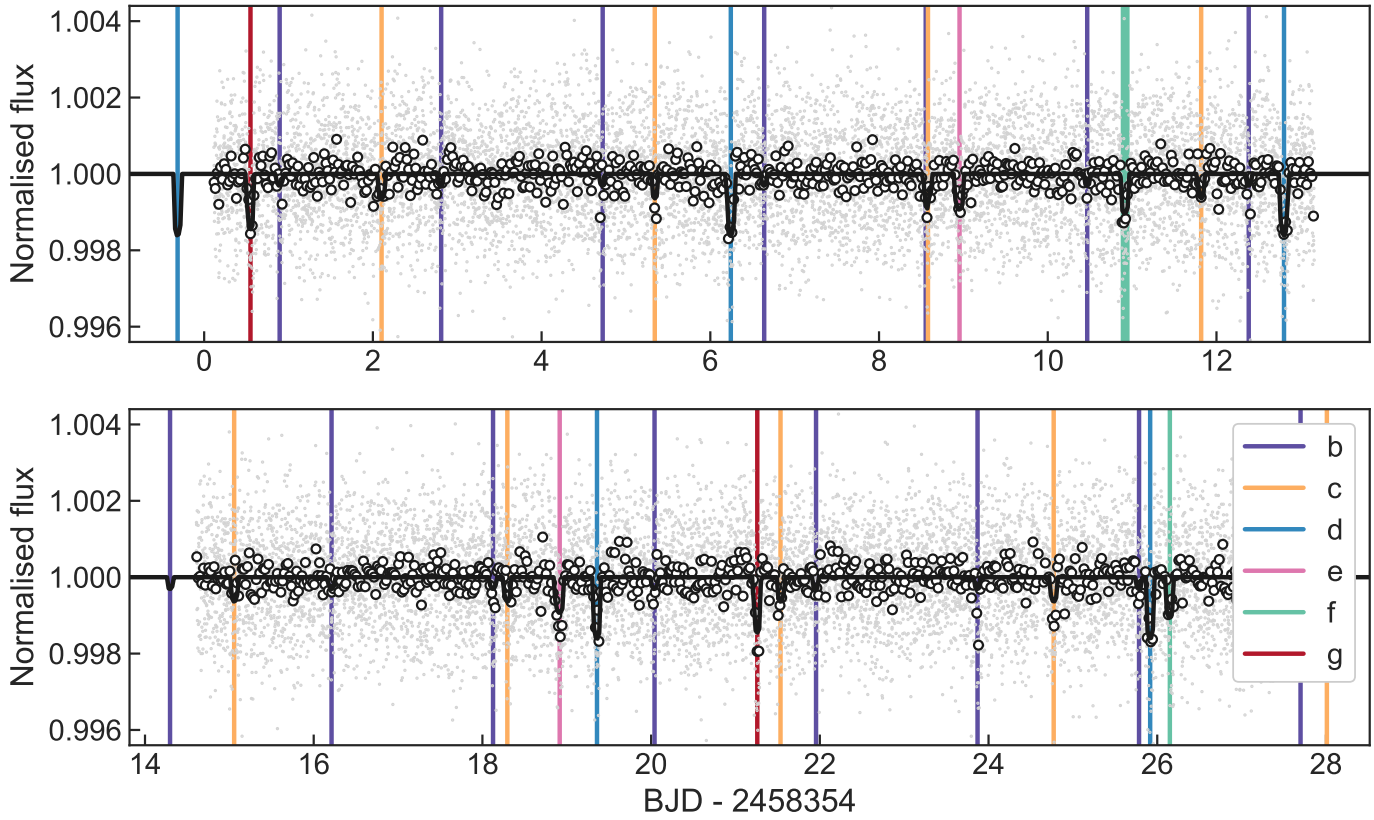

Fig. 1: Light curves from TESS Sector 2 described in Sections 2 and 4.1.1. Unbinned data are shown as grey points, and data in 30 minutes bins are shown as black circles. The best fitting transit model for the system is shown in black, with the associated parameter values shown in Tables 3 and 4. The positions of the transits are marked with coloured lines according to the legend. The photometry before and after the mid-sector gap are shown in the top and bottom panels, respectively. As the first transit of planet f (thick teal line) occurred precisely between the two transits of the similarly-sized planet g (period of 20.71 d - red lines), the three transits were originally thought to have arisen due to a single planet, which was originally designated TOI-178.02 with a period of 10.35 d (see section 2).

$P = 20.7$ d planet would not transit during the September 2019 observation window. Using the ephemerides from fitting the TESS, NGTS, and SPECULOOS data, we predicted the mid-transit of the 20.7 days candidate to occur between UTC 14:06 and 14:23 on 2020-September-07 with 98% certainty. A third visit of *CHEOPS* observed the system around this epoch for 13.36 h and confirmed the presence of this new planet (g) at the predicted time, with consistent transit parameters. Further analysis of all available photometric data found two possibilities for the unknown period of the additional planet: $\sim$ 12.9 d or $\sim$ 15.24 d.

Careful analysis of the whole system additionally revealed that planets *c*, *d*, *e* and *g* were in a Laplace resonance. In order to fit in the resonant chain, the unknown period of the additional planet could have only two values: $P = 13.4527$ d, or $P = 15.2318$ d, the latter value being also more consistent with the RV data. A fourth *CHEOPS* visit was therefore scheduled on Oct. 03 and detected the transit for the additional planet at a period of $15.23186^{+0.00011}_{-0.00012}$ day.

As we will detail in the next sections, using the new observations presented in this paper we can confirm the detection of a 6.56 and 9.96 d period planets by *TESS*, and announce the detection of planets at 1.91, 3.24, 15.23, and 20.71 d (see Tables 3 and 4 for all the parameters of the system).

3. TOI-178 Stellar Characterisation

Forty-six ESPRESSO observations (see Sect. 4.2) of TOI-178, a V = 11.95 mag K-dwarf, have been used to determine the stellar spectral parameters. These observations have first been shifted and stacked to produce a combined spectrum. We have then used the publicly available spectral analysis package `SME` (Spectroscopy Made Easy; Valenti & Piskunov 1996; Piskunov & Valenti 2017) version 5.22 to model the co-added ESPRESSO spectrum. We selected the ATLAS12 model atmospheres grids (Kurucz 2013) and atomic line data from VALD to compute synthetic spectra which was fitted to the observations using a χ^2-minimising procedure. We modelled different spectral lines to obtain different photospheric parameters and started with the line wings of Hα which are particularly sensitive to the stellar effective temperature $T_{\rm eff}$. We then proceeded with the metal abundances and the projected rotational velocity $v \sin i_\star$ which were modelled with narrow lines between 5900 and 6500 Å. We found similar values for [Fe/H], [Ca/H], and [Na/H]. The macro- and micro turbulent velocities were fixed to 1.2 km s^{-1} and 1.0 km s^{-1}, respectively, and mod-

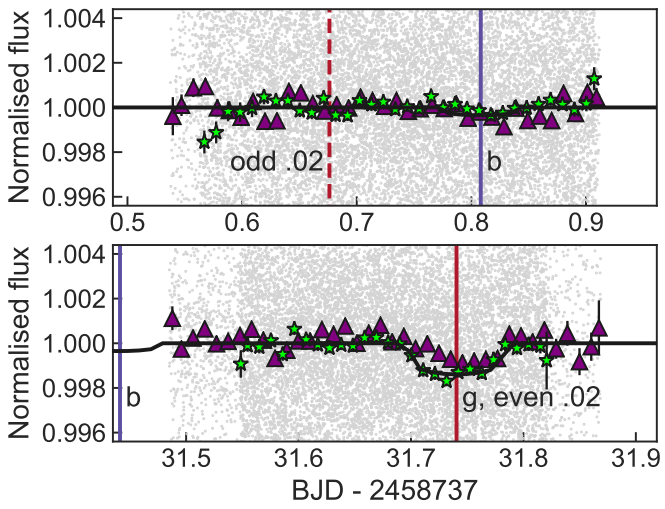

Fig. 2: Light curves from simultaneous observations of TOI-178 by NGTS (green stars) and SPECULOOS-South (purple triangles), described in sections 4.1.3 and 4.1.4, respectively. Unbinned data are shown as grey points, and data in 15 minute bins are shown as green stars (NGTS) and purple triangles (SPECULOOS). The observations occurred on 2019-September-11 (top panel) and 2019-October-12 (bottom panel). The transit model is shown in black. The position of the odd transit of candidate TOI-178.02 is shown with a dashed red line, the transit of planet g (which corresponds to an even transit of TOI-178.02) is shown with the solid red line, and the transits of planet b are shown with purple lines.

Table 1: Stellar properties of TOI-178 including the methods used to derive them.

TOI-178		
2MASS	J00291228-3027133	
Gaia DR2	2318295979126499200	
TIC	251848941	
TYC	6991-00475-1	
Parameter	Value	Note
α [J2000]	$00^h29^m12.30^s$	1
δ [J2000]	$-30°27'13.46''$	1
μ_α [mas/yr]	149.95±0.07	1
μ_δ [mas/yr]	-87.25±0.04	1
ϖ [mas]	15.92±0.05	1
RV [km s^{-1}]	57.4±0.5	1
V [mag]	11.95	2
G [mag]	11.15	1
J [mag]	9.37	3
H [mag]	8.76	3
K [mag]	8.66	3
$W1$ [mag]	8.57	4
$W2$ [mag]	8.64	4
$T_{\rm eff}$ [K]	4316±70	spectroscopy
$\log g$ [cgs]	4.45±0.15	spectroscopy
[Fe/H] [dex]	-0.23±0.05	spectroscopy
$v \sin i_\star$ [km s^{-1}]	1.5±0.3	spectroscopy
$R_\star$ [$R_\odot$]	0.651±0.011	IRFM
$M_\star$ [$M_\odot$]	$0.647^{+0.035}_{-0.032}$	isochrones
$t_\star$ [Gyr]	$7.1^{+6.2}_{-5.4}$	isochrones
$L_\star$ [$L_\odot$]	0.132±0.010	from $R_\star$ and $T_{\rm eff}$
$\rho_\star$ [$\rho_\odot$]	2.35±0.17	from $R_\star$ and $M_\star$

Notes. [1] Gaia Collaboration et al. (2018), [2] Høg et al. (2000), [3] Skrutskie et al. (2006), [4] Wright et al. (2010)

elled with a radial-tangential profile. The surface gravity $\log g$ was constrained from the line wings of the Ca I triplet (6102, 6122, & 6162 Å) and the Ca I 6439 Å line with a fixed $T_{\rm eff}$ and Ca abundance.

We checked our model with the Na I doublet sensitive to both $T_{\rm eff}$ and $\log g$, and finally we also tested the MARCS 2012 (Gustafsson et al. 2008) model atmosphere grids. The derived and finally adopted parameters are listed in Table 1. The `SME` results are in agreement with the empirical `SpecMatch-Emp` (Yee et al. 2017) code which fits the stellar optical spectra to a spectral library of 404 M5 to F1 stars resulting in $T_{\rm eff} = 4316 \pm 70$ K, $\log g = 4.45 \pm 0.15$, and [Fe/H] $= -0.29 \pm 0.05$ dex. We also used ARES+MOOG (Sousa 2014; Sousa et al. 2015; Sneden 1973) to do the spectroscopic analysis on the same combined ESPRESSO spectra and although we derived consistent parameters ($T_{\rm eff} = 4499 \pm 227$ K, $\log g = 4.38 \pm 0.62$, and [Fe/H] $= -0.34 \pm 0.1$), the large errors are indicative of the difficulties that equivalent width methods have in colder stars as this one where more spectral lines are more crowded in the spectrum.

Using these precise spectral parameters as priors on stellar atmospheric model selection, we determined the radius of TOI-178 using the infrared flux method (IRFM; Blackwell & Shallis 1977) in a Markov-chain Monte Carlo (MCMC) approach. The IRFM computes the stellar angular diameter and effective temperature via comparison between observed broadband optical and infrared fluxes and synthetic photometry obtained from convolution of the considered filter throughputs, using the known zero-point magnitudes, with the stellar atmospheric model, with the stellar radius then calculated using the parallax of the star. For this study, we retrieved the *Gaia* G, $G_{\rm BP}$, and $G_{\rm RP}$, 2MASS J, H, and K, and *WISE* W1 and W2 fluxes and relative uncertainties from the most recent data releases (Skrutskie et al. 2006; Wright et al. 2010; Gaia Collaboration et al. 2018, respectively), and utilised the stellar atmospheric models from the ATLAS Catalogues (Castelli & Kurucz 2003), to obtain $R_\star = 0.651 \pm 0.011\,R_\odot$, and $T_{\rm eff} = 4352 \pm 52$ K, in agreement with the spectroscopic $T_{\rm eff}$ used as a prior.

We inferred the mass and age of TOI-178 using stellar evolutionary models, using as inputs Teff, $R_\star$ and Fe/H, with evolutionary tracks and isochrones generated by two grids of models separately; the PARSEC[1] v1.2S code (Marigo et al. 2017) and the CLES code (Code Liégeois d'Évolution Stellaire; Scuflaire et al. 2008), with the reported values representing a careful combination of results from both sets of models. This was done as the sets of models differ slightly in approaches (reaction rates, opacity and overshoot treatment, and helium-to-metal enrichment ratio), and thus by comparing masses and ages derived from both grids it is possible to include systematic uncertainties within modelling the position of TOI-178 on evolutionary tracks and isochrones. A detailed discussion of combining the PARSEC and CLES models to determine masses and

[1] Padova and Trieste Stellar Evolutionary Code `http://stev.oapd.inaf.it/cgi-bin/cmd`.

ages can be found in Bonfanti et al. (*submitted*). For this study we derive $M_\star = 0.647^{+0.035}_{-0.032}\,M_\odot$ and $t_\star = 7.1^{+6.2}_{-5.4}$ Gyr. All stellar parameters are shown in Table 1.

4. Data

4.1. Photometric data

In order to determine the orbital configuration of the TOI-178 planetary system we obtained photometric time-series observations from multiple telescopes, as detailed below.

4.1.1. TESS

Listed as TIC 251848941 in the *TESS* Input Catalog (TIC; Stassun et al. 2018, 2019), TOI-178 was observed by *TESS* in Sector 2, camera 2 from 2018-August-22 to 2018-September-20. The individual frames were processed into 2 minute cadence observations and reduced by the Science Processing Operations Center (SPOC; Jenkins et al. 2016) into light curves made publicly available at the Mikulski Archive for Space Telescopes (MAST). For our analysis we retrieved the Presearch Data Conditioning Single Aperture Photometry (PDCSAP) light curve data, using the default quality bitmask, that has undergone known systematic correction (Smith et al. 2012; Stumpe et al. 2014). Lastly, we rejected data points flagged as of bad quality by the SPOC (`QUALITY` > 0) and those with Not-a-Number flux or flux error values. After these quality cuts, the *TESS* light curve of TOI-178 contained 18,316 data points spanning 25.95 d. The full dataset with the transits of the six identified planets is shown in Fig. 1.

4.1.2. CHEOPS

CHEOPS, the first ESA small-class mission, is dedicated to the observation of bright stars ($V \lesssim 12$ mag) that are known to host planets and performs ultra high-precision photometry, with the precision being limited by stellar photon noise of 150 ppm/min for a $V = 9$ magnitude star. The *CHEOPS* instrument is composed of a f/8 Ritchey-Chretien on-axis telescope (∼30 cm diameter) equipped with a single frame-transfer back-side illuminated CCD detector. The satellite was successfully launched from Kourou (French Guiana) into a ∼700 km altitude Sun-synchronous orbit on December 18th 2019. *CHEOPS* took its first image on February 7th 2020 and, after passing the In-Orbit Commissioning (IOC) phase, routine operations started on March 25th 2020. More details on the mission can be found in Benz et al. (2020), and the first results have recently been presented in Lendl et al. (2020).

The versatility of the *CHEOPS* mission allows for space-based follow-up photometry of planetary systems identified by the *TESS* mission. This is particularly useful to complete the inventory of multi-planetary systems whose outer transiting planets have periods beyond ∼10 days.

We obtained four observation runs (or visits) of TOI-178 with *CHEOPS* between 2020-August-04 and 2020-October-03 as part of the Guaranteed Time, totalling 11.88 days on target with the observing log shown in Table 2. The majority of this time was spent during the first two visits (with lengths of 99.78 h and 164.06 h respectively) that were conducted sequentially from 2020-August-04 to 2020-August-15 so to achieve a near continuous 11 day photometric time series. The runs were split due to scheduling constraints with 0.84 h gap between visits. The third and fourth visits were conducted to confirm the additional planets predicted in the scenario presented in Section 2. They took place on 2020-September-07 and 2020-October-03, and lasted for 13.36 h and 8.00 h, respectively.

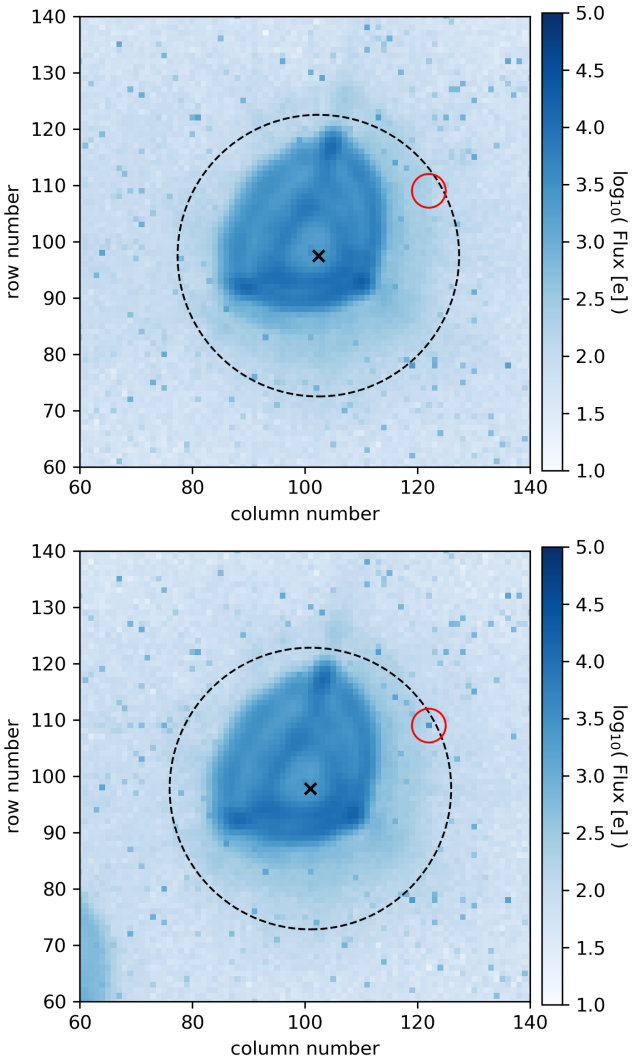

Fig. 3: Extraction of 80×80 arcsec of the *CHEOPS* Field-of-View for two different data frames at the beginning (top) and the end (bottom) of the second visit (see Table 2). The TOI-178 PSF is shown at the center with the DEFAULT DRP photometric aperture represented by the dashed black circles. The telegraphic pixel location which appeared close to the end of the observation is marked by the red circle.

Due to the low-Earth orbit of *CHEOPS*, the spacecraft-target line of sight was interrupted by Earth occultations, and along with passages through the South Atlantic Anomaly (SAA) where no data were downlinked. This resulted in gaps in the photometry on *CHEOPS* orbit timescales (around 100 min). For our observations of TOI-178, this resulted in light curve efficiencies of 51%, 54%, 65%, and 86%. For all four visits we used an exposure time of 60 s.

These data were automatically processed with the latest version of the *CHEOPS* data reduction pipeline (DRP

v12; Hoyer et al. 2020). This includes performing image calibration (bias, gain, non-linearity, dark current, and flat field), and conducting instrumental and environmental corrections (cosmic rays, smearing trails of field stars and background). It also performs aperture photometry for a set of size-fixed apertures: R=22.5″(RINF), 25″(DEFAULT) and 30″(RSUP), plus one extra aperture which minimizes the contamination from nearby field stars (ROPT) which in the case of TOI-178 was set in R=28.5″. The DRP estimates the level of contamination by simulating the Field-of-View of TOI-178 using GAIA star catalogue (Gaia Collaboration et al. 2018) to determinate the location and flux of the stars through the duration of the visit. In the case of TOI-178, the mean contamination level was below the 0.1% and modulated mostly by the rotation around the target of a nearby star of Gaia G=13.3 mag at a projected sky distance of 60.8″from the target. The contamination as a function of time (or equivalently as a function of roll angle of the satellite) is provided as a product of the DRP for further detrending (see Sect.5.1). For the second visit, careful removal of one *telegraphic* pixel (a pixel with an non-stable abnormal behaviour during the visit) within the photometric aperture was needed. The location of this telegraphic pixel is shown in red in Fig.3, and details on the detection and correction are described in Appendix A. Following the reductions, we found that the light curves obtained using the DEFAULT aperture (R=25″) yielded the lowest RMS for all visits and so are used for this study.

Lastly, it has become apparent that due to the nature of the *CHEOPS* orbit and rotation of the *CHEOPS* field, photometric, non-astrophysical short-term trends either from a varying background, nearby contaminating source or other sources, can be found in the data on orbital timescales. These systematics can be successfully removed via a linear detrending method against basis vectors of concern (e.g. Lendl et al. 2020, Bonfanti et al. *submitted*, Delrez et al. *submitted*). In this study we carefully inspected the light curves, and determined that by decorrelating the light curve against background and contamination estimates, and against *CHEOPS* roll angle, any remaining systematics were removed. For the final run, the background was heavily influenced by scattered light from the Moon and thus, this glint contribution was fitted by a N = 40 spline as an additional basis vector within the detrending and removed. Following this, the average noise over a 3 h sliding window for the four visits of the G = 11.15 mag target was found to be 63.9, 64.2, 66.3, and 75.8 ppm respectively. In all cases, this marginally improved upon the precision of the light curves that we had previously simulated for these observation windows using the `CHEOPSim` tool (Futyan et al. 2020).

4.1.3. NGTS

The Next Generation Transit Survey (NGTS; Wheatley et al. 2018) facility consists of twelve 20 cm diameter robotic telescopes and is situated at the ESO Paranal Observatory in Chile. The individual NGTS telescopes have a wide field-of-view of 8 square-degrees and a plate scale of $5\,''\,\mathrm{pixel}^{-1}$. The DONUTS auto-guiding algorithm (McCormac et al. 2013) affords the NGTS telescopes sub-pixel level guiding. Simultaneous observations using multiple NGTS telescopes have been shown to yield ultra-high precision light curves of exoplanet transits (Bryant et al. 2020; Smith et al. 2020).

TOI-178 was observed using NGTS multi-telescope observations on two nights. On UT 2019 September 10 TOI-178 was observed using six NGTS telescopes during the predicted transit event of the TESS candidate TOI-178.02. However, the NGTS data for this night rule out a transit occurring during the observations. A second predicted transit event of TOI-178.02 was observed on the night UT 2019 October 11 using seven NGTS telescopes, and on this night the transit event was robustly detected by NGTS. A total of 13,991 images were obtained on the first night, and 12,854 were obtained on the second. For both nights the images were taken using the custom NGTS filter (520 - 890 nm) with an exposure time of 10 s. All NGTS observations of TOI-178 were performed with airmass < 2 and under photometric sky conditions.

The NGTS images were reduced using a custom pipeline which uses the `SEP` library to perform source extraction and aperture photometry (Bertin & Arnouts 1996; Barbary 2016). A selection of comparison stars with brightness, colour, and CCD position similar to TOI-178 were identified using GAIA DR2 (Gaia Collaboration et al. 2018). More details on the photometry pipeline are provided in Bryant et al. (2020).

The NGTS light curves are presented in Fig. 2, and show transit events for planet b and planet g on the nights of 2019 September 11 and 2019 October 1 respectively.

4.1.4. SPECULOOS

The SPECULOOS Southern Observatory (SSO; Gillon 2018; Burdanov et al. 2018; Delrez et al. 2018) is located at ESO's Paranal Observatory in Chile and is part of the SPECULOOS project. The facility consists of a network of four robotic 1-m telescopes (Callisto, Europa, Ganymede, and Io). Each SSO robotic telescope has a primary aperture of 1 m and a focal length of 8 m, and is equipped with a 2k×2k deep-depletion CCD camera whose 13.5 μm pixel size corresponds to 0.35" on the sky (field of view = 12′x12′). Observations were performed on the nights starting the 10th of October 2019 (for $\simeq$ 8 hours) and the 11th of November 2019 (for $\simeq$ 8 hours) with three SPECULOOS telescopes on sky simultaneously (SSO/Io, SSO/Europa, and SSO/Ganymede). These observations were carried out in a Sloan i' filter with exposure times of 10 s. A small defocus was applied to avoid saturation as the target was too bright for SSO. Light curves were extracted using the SSO pipeline (Murray et al. 2020) and shown in purple on Fig.2. For each observing night, the SSO pipeline uses the `casutools` software (Irwin et al. 2004) to perform automated differential photometry and correct from systematics caused by time-varying telluric water vapor.

4.2. ESPRESSO Data

The radial velocity data we analyse consists in 46 ESPRESSO points[2]. Each measurement is taken in HR mode with an integration time of 20 min in single UT mode and slow read-out (HR 21). The source on fiber B is the Fabry-Perot interferometer. Observations were made with a maximum airmass of 1.8 and minimum 30° separation with the Moon.

[2] The first 32 ones come from program 0104.C-0873(A), the last 14 from guaranteed time observations.

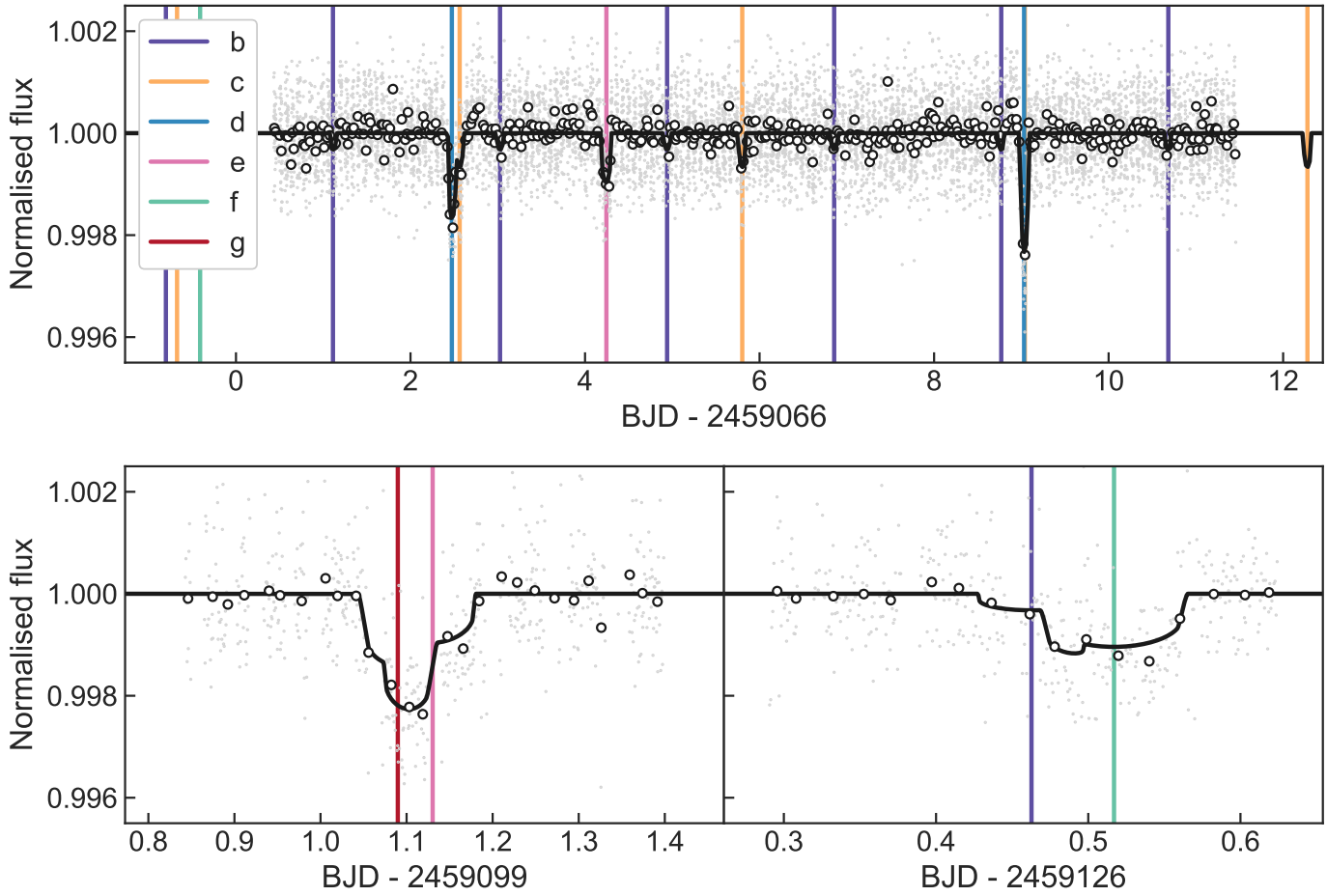

Fig. 4: Similar to Fig. 1, but instead displaying data from the four CHEOPS visits described in 4.1.2. Top panel: the 11 d observation. Transits of planets c and d at ∼ 2459075 BJD occur too close for their corresponding lines to be individually visible in the figure. Bottom left panel: subsequent observation scheduled to confirm the presence of a planet with a 20.7 d period (planet g), which overlaps with a transit of planet e. Bottom right panel: final observation scheduled to confirm the presence of a planet fitting in the Laplace resonance (planet f, with a period of ∼15.23 d period), which overlaps with a transit of planet b.

Table 2: The log of *CHEOPS* observations of TOI-178.

visit #	Identified planets	Start date [UTC]	Duration [h]	Data points [#]	File key	Efficiency [%]	Exp. Time [s]
1	b,c,d,e	2020-08-04T22:11:39	99.78	3030	CH_PR100031_TG030201_V0100	51	60
2	b,c,d	2020-08-09T02:48:39	164.04	5280	CH_PR100031_TG030301_V0100	54	60
3	e,g	2020-09-07T08:06:44	13.36	521	CH_PR100031_TG030701_V0100	65	60
4	b,f	2020-10-03T18:51:46	8.00	413	CH_PR100031_TG033301_V0100	86	60

The measurements span from 29 Sep. 2019 to 20 Jan. 2020 and have an average nominal error bar of 93 cm/s. We also include in our analysis the time-series of $H\alpha$ measurements, the full width half maximum (FWHM) and the S-index. The velocity and ancillary indicators are extracted from the spectra with the standard ESPRESSO pipeline v 2.0.0 (Pepe et al. 2020). The RV time-series with nominal error bars is shown in Fig. 5.

5. Detections and parameters estimations

We analyse the photometric and spectral data separately and jointly, which we describe in the following sections. This approach allows us to independently detect the planets in the system, and subsequently verify them in a global fit.

5.1. Analysis of the photometry

5.1.1. Identification of the solution

The first release of candidates from the *TESS* alerts of Sector 2 included three planet candidates in TOI-178 with periods of 6.55 d, 10.35 d, and 9.96 d, which transited 4, 3, and 2 times, respectively. In addition, our analysis of this dataset with the DST (Cabrera et al. 2012) yielded two additional candidates, a clear 3.23 d signal, and a fainter 1.91 d one. Upon receiving the visits 1 and 2 from *CHEOPS* (Table 2),

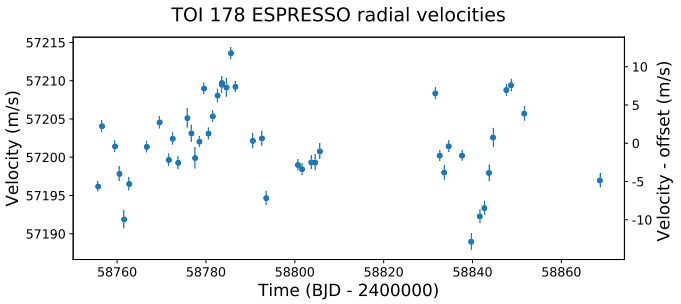

Fig. 5: ESPRESSO RV data of TOI-178.

a study of the *CHEOPS* data alone with successive applications of the BLS algorithm (Kovács et al. 2002) retrieved the 6.55 d 3.23 d, and 1.91 d signal in phase agreement with the *TESS* data. An additional dim, consistent in epoch with a transit of the 9.9 d candidate was also identified, but could also have marginally correspond to a transit of the 10.35 d candidate.

Taking *TESS* sector 2, NGTS visits of September and October 2019, and *CHEOPS* visits 1 and 2, we individually pre-detrended the datasets and subtracted the signal of the 6.55 d 3.23 d, and 1.91 d candidates. We then applied the BLS algorithm a first time on this dataset, saved the most likely candidate of period P_1, and removed the corresponding signal, and applied the BLS a second time to obtain a second candidate of period P_2. That created a first pair of candidates $c_{0,0}$. We then repeated this process, but ignoring the result of the BLS for periods less that 0.2 d away from P_1 for the first candidate of the pair, while taking the highest peak on the second iteration of the BLS, leading to the pair $c_{1,0}$. We repeated this process 25 times, yielding to 25 potential pairs of candidates $c_{0\leq i\leq 4,0\leq j\leq 4}$, where i and j are the number of peaks that have been ignored in the first or second iteration of the BLS, respectively. For all of these potential solutions we modeled the transits of the 5 candidates : 1.91 d, 3.23 d, 6.55 d, and $c_{i,j}$; using the `batman` package (Kreidberg 2015) and ran an MCMC on the pre-detrended lightcurve to estimate the relative likelihood of the different $c_{i,j}$. The 1.91 d, 3.23 d, 6.55 d, 9.96 d, and 20.71 d model was favoured, and explained all the significant dims observed in the NGTS/SPECULOOS data (Fig. 2) and the first visit of *CHEOPS* (Fig. 4 - *top*). This solution was later confirmed by the predicted double transit observed by the 3rd visit of *CHEOPS* (Fig. 4 - *bottom left*).

Applying the BLS algorithm on the residuals of the available photometric data, Two mutually exclusive peaks appeared: $\sim$ 12.9 d and $\sim$ 15.24 d, the former being slightly favoured by the BLS analysis. However, the global fit of the lightcurve favoured the $\sim$ 15.24 d signal. In addition, this solution was very close to the period that would fit the resonant structure of the system, see section 6. The $\sim$ 15.24 d candidate was confirmed by a 4th *CHEOPS* visit (Fig. 4 - *bottom right*). In the next section we develop the characterisation of this 6-planets solution: 1.91 d, 3.23 d, 6.55 d, 9.96 d, $\sim$ 15.24 and 20.71 d.

5.1.2. Determination of radii and orbital parameters

To detect orbiting bodies, and characterise the system we performed a fit of the *TESS*, NGTS, and *CHEOPS* photometry. As the NGTS and SPECULOOS data presented in Fig. 2 cover the same epoch of observations, we only included the NGTS data in our fit as it had a smaller RMS photometric scatter.

The fit was performed using the `allesfitter` package (Günther & Daylan 2020). Wide, uniform priors for each planet were placed on the transit parameters $R_p/R_\star$, $(R_\star + R_p)/a$, $\cos i$, T_0, and P; where R_p and $R_\star$ are respectively the radii of the planet and star, a is the semi-major axis, i is the orbital inclination, T_0 is the time of inferior conjunction, and P is the period. Gaussian priors with $\sigma = 0.1$ were placed on the quadratic limb darkening parameters q_1 and q_2 (the parameterisation given by Kipping 2013) for each instrument, with the mean values calculated according to Claret & Bloemen (2011). We also placed a uniform prior on $\rho_\star$, calculated as described in section 3. The eccentricity and argument of periastron components for each planet used in the fitting was fixed to 0, as justified in section 6.3.

Systematic trends were removed from the CHEOPS light curves before their inclusion in the global fit using the `pycheops` package (Maxted et al., *in prep.*). Each visit was detrended using a set of linear basis vectors that optimised the Bayesian Evidence Z (chosen from background, contamination, linear and quadratic functions of detection xy position, and trigonometric functions of roll angle). Due to the small angular separation of the moon for the final visit, we also detrending with a linear basis vector constructed from a spline function fit fitting the flux as a function of roll angle, centred on the direction of the moon.

The time correlated trends in the *TESS* light curve were modelled simultaneously with the transit parameters using a Gaussian process with a Matérn 3/2 kernel which is implemented in `allesfitter` using the `celerite` package (Foreman-Mackey et al. 2017a). The natural logarithms of the hyperparameters were allowed to vary between -5 and 5 for $\log(\sigma)$ and 5 and 15 for $\log(\rho)$.

The best-fitting values and uncertainties associated with each parameter were calculated using dynamic nested sampling, which is implemented in `allesfitter` using the `dynesty` package. The best-fitting transit parameters associated with each of the planet are displayed in Table 4.1.

The results from the model are displayed in Tables 3 and 4.

This analysis yields a solution of the system that is best explained by 6 signals of planetary nature:

- a 275 ppm signal of 1.65 h duration, with a time of conjunction of 2458741.6371 BJD, and a period of 1.914557 d.
- a 580 ppm signal of 1.89 h duration, with a time of conjunction of 2458741.4790 BJD, and a period of 3.238458 d.
- a 1383 ppm signal of 2.280 h duration, with a time of conjunction of 2458747.1465 BJD, and a period of 6.557694 d.
- a 934 ppm signal of 2.45 h duration, with a time of conjunction of 2458751.4661 BJD, and a period of 9.961872 d.
- a 1123 ppm signal of 2.356 h duration, with a time of conjunction of 2458745.7177 BJD, and a period of 15.231930 d.
- a 1679 ppm signal of 2.189 h duration, with a time of conjunction of 2458748.0293 BJD, and a period of 20.709460 d.

Table 3: Fitted and derived results for planets b, c, and d associated with the fits to the photometry and spectroscopy described in sections 5.1 and 5.2, respectively.

Parameter (unit)	b	c	d
Fitted parameters (photometry)			
$R_\mathrm{p}/R_\star$	0.01658 ± 0.00098	$0.0241^{+0.0012}_{-0.0011}$	0.03719 ± 0.00074
$(R_\star + R_\mathrm{p})/a$	$0.1181^{+0.0028}_{-0.0026}$	$0.0836^{+0.0018}_{-0.0017}$	$0.0530^{+0.0014}_{-0.0012}$
$\cos i$	0.035 ± 0.021	$0.034^{+0.013}_{-0.017}$	0.0272 ± 0.0027
t_0 (BJD-TBD)	$2458741.6371^{+0.0037}_{-0.0030}$	2458741.4790 ± 0.0025	$2458747.14645^{+0.00071}_{-0.00075}$
P (d)	$1.914557^{+0.000016}_{-0.000018}$	$3.238458^{+0.000020}_{-0.000018}$	6.557694 ± 0.000013
Fitted parameters (spectroscopy)			
K (ms^{-1})	$1.05^{+0.25}_{-0.30}$	$2.77^{+0.22}_{-0.33}$	$1.34^{+0.31}_{-0.39}$
Derived parameters			
δ_tr (ppm)	275^{+32}_{-31}	580^{+60}_{-52}	1383^{+55}_{-54}
$R_\star/a$	$0.1162^{+0.0028}_{-0.0025}$	$0.0816^{+0.0018}_{-0.0017}$	$0.0511^{+0.0014}_{-0.0012}$
$a/R_\star$	8.61 ± 0.20	12.25 ± 0.27	$19.58^{+0.46}_{-0.51}$
R_p/a	$0.00193^{+0.00012}_{-0.00011}$	$0.001965^{+0.00012}_{-0.000097}$	$0.001899^{+0.000074}_{-0.000066}$
R_p ($\mathrm{R}_\oplus$)	1.177 ± 0.074	$1.710^{+0.094}_{-0.082}$	2.640 ± 0.069
a (AU)	0.02604 ± 0.00075	0.0371 ± 0.0010	0.0592 ± 0.0018
i (deg)	88.0 ± 1.2	$88.04^{+0.97}_{-0.74}$	88.44 ± 0.16
b	0.30 ± 0.18	$0.42^{+0.15}_{-0.21}$	$0.532^{+0.041}_{-0.043}$
t_{14} (h)	$1.649^{+0.064}_{-0.11}$	$1.89^{+0.13}_{-0.17}$	2.054 ± 0.043
t_{23} (h)	$1.590^{+0.067}_{-0.12}$	$1.78^{+0.14}_{-0.18}$	2.054 ± 0.043
T_eq (K)	952 ± 19	798 ± 16	631 ± 13
M_p ($\mathrm{M}_\oplus$)	$1.51^{+0.38}_{-0.45}$	$4.76^{+0.55}_{-0.67}$	$2.90^{+0.72}_{-0.92}$
ρ_p ($\rho_\oplus$)	$0.91^{+0.26}_{-0.33}$	$0.90^{+0.16}_{-0.21}$	$0.15^{+0.03}_{-0.04}$

We denote this series of planetary signals respectively as TOI-178 b, c, d, e, f, and g.

The signals were detected with SNRs of 8.47, 9.72, 25.23, 15.61, 15.2, and 14.52, respectively, with the number of transits for each planetary signal being: 19, 11, 6, 4, 3, and 4. When incorporating the stellar radius calculated as described in section 3, the planets have radii of 1.177, 1.710, 2.640, 2.169, 2.379, and 2.91 $R_\oplus$, with the inner two planets falling either side of the radius valley (Fulton et al. 2017).

The transits of all detected planets are shown in Figs. 1 and 4, with the phase folded transits in the *CHEOPS* data presented in Fig. 6.

5.2. Analysis of the radial velocities

5.2.1. Detections

In this section, we consider the forty-six ESPRESSO data points only, and look for potential planet detections. Our analysis follows the same steps as Hara et al. (2020), and is described in detail in Appendix B. To search for potential periodicities, we computed the ℓ_1 periodogram[3] of the RV, as defined in Hara et al. (2017). This method outputs a figure which has a similar aspect as a regular periodogram, but with fewer peaks due to aliasing. The peaks can be assigned a false alarm probability (FAP), whose interpretation is close to the FAP of a regular periodogram peak.

A preliminary analysis of ancillary indicators $H\alpha$, FWHM, bisector span (Queloz et al. 2001) and $\log R'_{HK}$ (Noyes 1984) revealed that they exhibit statistically significant periodicities at ≈ 36 days and ≈ 16 days, such that stellar activity effects are to be expected in the RVs, especially at these periods. In our analysis, stellar activity has been taken into account both with a linear model constructed with activity indicators smoothed with a Gaussian process regression similarly to Haywood et al. (2014), which we call the base model, and with a Gaussian noise model with a white, correlated (Gaussian kernel) and quasi periodic component.

Radial velocity signals found to be statistically significant might vary from one activity model to another. To announce robust detections, we tested whether signal detections can be claimed for a variety of noise models, following Hara et al. (2020). This approach consists in three steps. First, we computed ℓ_1-periodogram of the data on a grid of models. The linear base models considered include an offset and smoothed ancillary indicators ($H\alpha$, FWHM, none or both), where the smoothing is done with a Gaussian process regression with a Gaussian kernel. The noise models considered are Gaussian with three components: white, red with Gaussian kernel, and quasi-periodic. According to the analysis of ancillary indicators, the quasi-periodic term of the noise is fixed at 36.5 days. We consider a grid of values for each noise component (amplitude, decay time-scale), and compute the ℓ_1-periodograms. Secondly, we rank the noise models with a procedure based on cross-validation. Finally, we examine the distribution of FAPs of each signal in the 20% highest ranked models

We here succinctly describe the conclusions of our analysis, and refer the reader to Appendix B for a more detailed presentation. The ℓ_1-periodogram corresponding to the highest ranked model is represented in Fig. 7. The periods at which the peaks occur are shown in red, and account for most of the signals that might appear with varying assumptions on the noise/activity model. More precisely, we find the following results. Note that these ones stem from

[3] https://github.com/nathanchara/l1periodogram

Table 4: Fitted and derived results for planets e, f, and g associated with the fits to the photometry and spectroscopy described in sections 5.1 and 5.2, respectively.

Parameter (unit)	e	f	g
Fitted parameters (photometry)			
$R_p/R_\star$	$0.03057^{+0.00091}_{-0.00098}$	0.0335 ± 0.0011	0.0410 ± 0.0014
$(R_\star + R_p)/a_p$	$0.03989^{+0.00098}_{-0.00091}$	$0.03001^{+0.00070}_{-0.00065}$	0.02462 ± 0.00056
$\cos i$	$0.0233^{+0.0020}_{-0.0025}$	0.02214 ± 0.00100	$0.02036^{+0.00068}_{-0.00064}$
T_0 (BJD-TBD)	$2458751.4661^{+0.0014}_{-0.0019}$	$2458745.7177^{+0.0021}_{-0.0025}$	$2458748.0293^{+0.0014}_{-0.0012}$
P (d)	$9.961872^{+0.000034}_{-0.000038}$	$15.231930^{+0.00011}_{-0.000085}$	$20.709460^{+0.000077}_{-0.000069}$
Fitted parameters (spectroscopy)			
K (ms^{-1})	$1.62^{+0.41}_{-0.34}$	$2.76^{+0.46}_{-0.42}$	$1.30^{+0.38}_{-0.59}$
Derived parameters			
δ_{tr} (ppm)	934^{+56}_{-60}	1123^{+70}_{-71}	1680^{+110}_{-120}
$R_\star/a$	$0.03871^{+0.00094}_{-0.00088}$	$0.02904^{+0.00068}_{-0.00063}$	0.02365 ± 0.00053
$a/R_\star$	25.83 ± 0.61	34.44 ± 0.79	42.28 ± 0.93
R_{p}/a	0.001183 ± 0.000052	$0.000973^{+0.000041}_{-0.000039}$	0.000969 ± 0.000043
R_{p} ($\mathrm{R}_\oplus$)	2.169 ± 0.079	2.379 ± 0.086	2.91 ± 0.11
a (AU)	0.0782 ± 0.0023	0.1042 ± 0.0029	0.1280 ± 0.0036
i (deg)	$88.67^{+0.14}_{-0.12}$	88.731 ± 0.057	$88.833^{+0.037}_{-0.039}$
b	$0.604^{+0.041}_{-0.060}$	$0.763^{+0.020}_{-0.022}$	$0.861^{+0.012}_{-0.014}$
t_{14} (h)	$2.455^{+0.12}_{-0.068}$	$2.356^{+0.063}_{-0.059}$	$2.189^{+0.060}_{-0.055}$
t_{23} (h)	$2.226^{+0.13}_{-0.079}$	$2.005^{+0.079}_{-0.075}$	1.579 ± 0.092
T_{eq} (K)	549 ± 11	475.8 ± 9.6	429.4 ± 8.5
M_{p} ($\mathrm{M}_\oplus$)	$4.04^{+1.07}_{-0.95}$	$7.94^{+1.45}_{-1.52}$	$4.14^{+1.26}_{-1.82}$
ρ_{p} ($\rho_\oplus$)	$0.39^{+0.12}_{-0.10}$	$0.58^{+0.13}_{-0.12}$	$0.19^{+0.05}_{-0.09}$

an analysis of over 1300 noise models, and are not all evident from Fig. 7, obtained with the highest ranked noise model.

- Our analysis yields consistent, significant detection of signals close to 3.2, ≈ 36 and ≈ 16 days. RV then allows an independent detection of planet c. Signals at ≈ 36 and ≈ 16 d appear in ancillary indicators, such that we attribute these apparent periodicities in RV to stellar activity. The 16 days signal is, however, very likely to be partly due to planet f. Indeed, when the activity signals close to 40 and 16 days are modelled and the signal of transiting planets is removed, one finds a residual signal at 15.1 or 15.2 days, even though 16 and 15.2 days are very close.
- We find signals, though not statistically significant, at 6.5 and 9.8 days (consistent with planets d and e) and 2.08 days, which is the one day alias (see Dawson & Fabrycky 2010) of 1.91 days (planet b).
- We do not consistently find a candidate near 20.7 days. However, a 20.6 days signal appears in the highest ranked model, and stellar activity signal might hide the signal corresponding to TOI-178 g.
- The signal at 43.3 days appearing in Fig. 7 might be a residual effect of an imperfect correction of the activity. It is however not strictly excluded that it might stem from a planetary companion at 45 days. As will be discussed in the conclusion, this period corresponds to one of the possibilities in order to continue the Laplace resonance beyond planet g.
- Depending on the assumptions, hints at 1.2 or 5.6 days (aliases of each other) can appear.

For comparison, we performed the RV analysis with an iterative periodogram approach. This one is able to show signals corresponding to 15.2, 3.2 and 6.5 days, however, this one is unable to clearly establish the significance of the 3.2 d signal, and fails to unveil candidates at 1.91 and 9.9 days.

The photometric data allows to independently detect six planets at 1.91, 3.24, 6.56, 9.96, 15.23 and 20.71 days.As detailed in Appendix B, wee find that the phases of RV and photometric signals are consistent within 2σ. We phase-fold the RV data at the periods given in Tables 3 and Tables 4, which are shown in Fig. 8 with increasing periods from top to bottom. The variations at 3.24 and 15.2 days, corresponding to the planets with the most significant RV signals, are the clearest. As a final remark, the signals corresponding to the transiting planets have been fitted, the strongest periodic signals occur at 38 and 16.3 days, which is compatible with the activity periods seen in the ancillary indicators.

5.2.2. Mass and density estimations

To estimate the planetary masses, we fit circular orbits to the radial velocities. As shown in section 6, for the system to be stable, eccentricities cannot be greater than a few percents. We set as priors on T_c and period the posterior distributions obtained from the fits to photometric data from Tables 3 and 4). This approach, as opposed to a joint fit, is justified by the fact that, here, RVs brings very little information to the parameters constrained by photometry and vice-versa. Activity signals clearly are present in the RV data, and depending on the activity model used, mass estimates may vary. To assess the model dependency of mass estimates, we use two different activity models. Both include as a linear predictor the smoothed $H\alpha$ time series, as described above. In the first model, we represent activ-

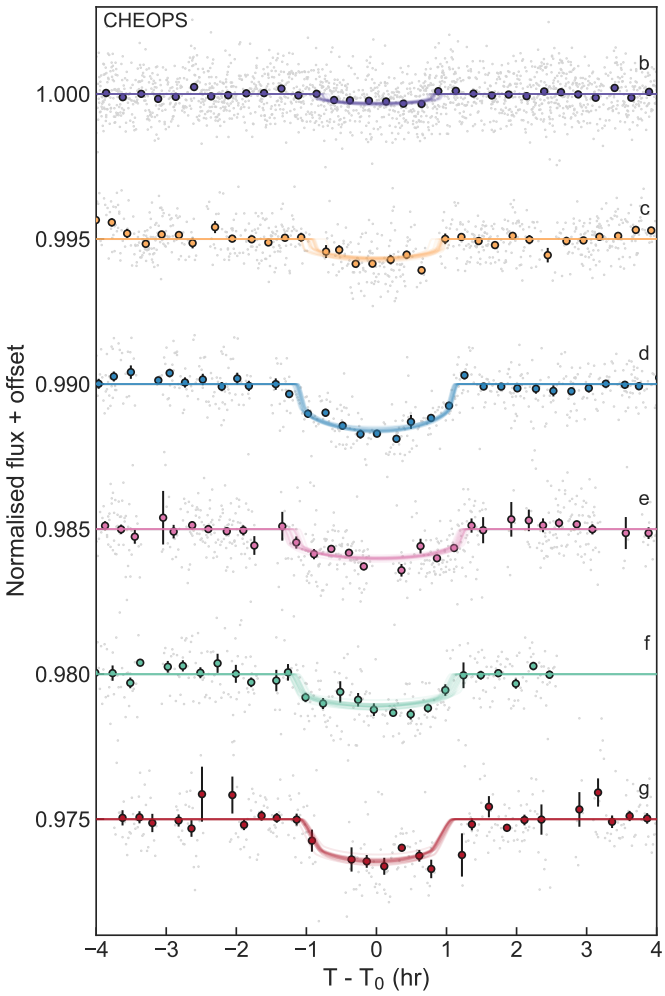

Fig. 6: Detrended CHEOPS light curves phase folded to the periods of each of the planets, with signals of the other planets removed. Unbinned data are shown in grey points, data in bins of 15 min are shown in coloured circles, and samples drawn from the posterior distribution of the global fit are shown in coloured lines.

ity as a sum of two sine functions at 36 and 16 days and a correlated noise with an exponential kernel. This is motivated by the fact that both periodicities appear the ancillary indicators, but with different phases. The correlated noise models low frequency variations, which also can be anticipated from the analysis of the indicators. The second model of activity consists of a correlated Gaussian noise with a quasi-periodic kernel. This analysis is presented in detail in Appendix B.5.

The mass estimation for each model are given in tables B.2, 3, and 4, respectively. The 1σ intervals obtained with the two methods all have a large overlap. In Tables 3 and 4, we give the mass and density intervals in a conservative manner. The lower and upper bounds are respectively taken as the minimum lower bound and maximum upper bound obtained with the two estimation methods. The mass estimates are given as the mean of the estimates obtained with the two methods, which are posterior medians. We take this approach and do not select the error bars of one model or another, since model comparisons heavily depend on prior chosen, which in our case would be rather

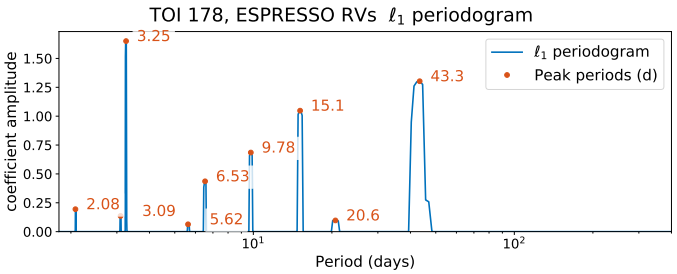

Fig. 7: ℓ_1 periodogram corresponding to the best noise models in terms of cross-validation score, computed on a grid of frequencies from 0 to 0.55 cycles per day.

Table 5: Instantaneous distance from resonances for the 6 planets of TOI-178, expressed in terms of near resonant angles ϕ. λ indicates the mean longitude of the planet specified in the subscript.

ϕ_i	$d\phi_i/dt$ [deg/day]	super period [day]
$\phi_0 = 3\lambda_b - 5\lambda_c$	$8.2811^{+0.0065}_{-0.0062}$	$43.472^{+0.033}_{-0.034}$
$\phi_1 = 1\lambda_c - 2\lambda_d$	$1.36886^{+7.8e-04}_{-7.6e-04}$	$262.99^{+0.15}_{-0.15}$
$\phi_2 = 2\lambda_d - 3\lambda_e$	$1.38188^{+9.4e-04}_{-9.7e-04}$	$260.52^{+0.18}_{-0.18}$
$\phi_3 = 2\lambda_e - 3\lambda_f$	$1.37131^{+8.0e-04}_{-7.8e-04}$	$262.52^{+0.15}_{-0.15}$
$\phi_4 = 3\lambda_f - 4\lambda_g$	$1.37050^{+6.0e-04}_{-6.0e-04}$	$262.68^{+0.12}_{-0.11}$

arbitrary. We find planet masses and density ranging from 1.5 to 8 $M_\oplus$ and 0.15 to 0.9 $\rho_\oplus$. Note that, even though two models are used to estimate stellar activities and give consistent estimates, the mass intervals might still evolve with as more data comes along and the results become less model-dependent. In particular, it seems like the mass of planet f, at 15.2 days, can be constrained despite activity signatures at 16 days. A longer baseline would nonetheless be suitable, so that the difference between 15.2 and 16 would be greater than the frequency resolution.

6. Dynamics

6.1. A Laplace resonant chain

MMRs are orbital configurations where the period ratio of a pair of planet is equal to, or oscillate around, a rational number of the form $(k+q)/k$, where k and q are integers. In TOI-178, the candidates b and c are close to a second order MMR ($q = 2$): $P_c/P_b = 1.6915 \approx 5/3$, while c, d, e, f and g are pairwise close to first-order mean motion resonances ($q = 1$): $P_d/P_c = 2.0249 \approx 2/1$, $P_e/P_d = 1.5191 \approx 3/2$, $P_f/P_e = 1.5290 \approx 3/2$ and $P_g/P_f = 1.3595 \approx 4/3$. Pairs of planets lying just outside MMRs are common occurrence in systems observed by transit (Fabrycky et al. 2014). To study such pair of planets, a relevant quantity is the distance to the exact resonance. Taking the pair c and d as example, the distance to the 2/1 MMR in the frequency space is given by $1n_c - 2n_d$, where $n_c = 2\pi/P_c$ is the mean motion of the planet c. Following Lithwick et al. (2012), we name 'super period' the associated timescale:

$$P_{c,d} \equiv \frac{1}{|(k+q)/P_d - k/P_c|} \,. \quad (1)$$

The values of these quantities are given in Table 5 for the planets b to g, along with the expression of the associ-

Table 6: Estimated values of the Laplace angles of planets c to g of TOI-178 toward the beginning of *TESS* Sector 2, at 2458350.0 BJD (August 2018). The derivative of the angles are averaged values between August 2018 and August 2020, based on the solution presented in tables 3 and 4. The equilibrium values of the Laplace angles are discussed in section 6.2

ψ_j	value [deg]	$d\psi_j/dt$ [deg/year]	equilibrium [deg]	distance from eq. [deg]
$\psi_1 = \phi_1 - \phi_2 = 1\lambda_c - 4\lambda_d + 3\lambda_e$	$166.70^{+0.82}_{-0.82}$	$-4.74^{+0.47}_{-0.48}$	180	$-13.30^{+0.82}_{-0.82}$
$\psi_2 = \phi_2 - \phi_3 = 2\lambda_d - 5\lambda_e + 3\lambda_f$	$157.57^{+1.16}_{-1.06}$	$3.86^{+0.58}_{-0.60}$	168.94 ± 7.79	$-11.37^{+7.88}_{-7.86}$
$\psi_3 = \frac{1}{2}(\phi_3 - \phi_4) = 1\lambda_e - 3\lambda_f + 2\lambda_g$	$71.98^{+0.38}_{-0.48}$	$0.15^{+0.23}_{-0.22}$	78.90 ± 1.23	$-6.92^{+1.29}_{-1.32}$

ated angles ϕ_i. TTVs are expected to happen over the super period, with amplitudes depending on the distance to the resonance, the mass of the perturbing planet and the eccentricities of the pair (Lithwick et al. 2012). The fact that the super period of all three of these pairs are close to the same value from planet c outward has additional implications : The difference between the angles ϕ_i is evolving very slowly. In other words, there is a Laplace relation between consecutive triplets:

$$\begin{aligned} d\psi_1/dt &= d(\phi_1 - \phi_2)/dt = 1n_c - 4n_d + 3n_e \approx 0\,, \\ d\psi_2/dt &= d(\phi_2 - \phi_3)/dt = 2n_d - 5n_e + 3n_f \approx 0\,, \\ d\psi_3/dt &= \frac{1}{2} d(\phi_3 - \phi_4)/dt = 1n_e - 3n_f + 2n_g \approx 0\,, \end{aligned} \tag{2}$$

implying that the system is in a 2:4:6:9:12 Laplace resonant chain. The values of the Laplace angles ψ_j and derivatives are given in table 6. The values of the ψ_j are instantaneous and computed at the date 2458350.0 BJD which is toward the beginning of the observation of TESS sector 2. As no significant TTVs were determined over the last two years, the derivatives of the ψ_j are average values over that period. The Laplace relations described in eq. (2) do not extend toward the innermost triplet of the system: according to equations (C.3 and C.4), $P_{b,c}$ should be equal to half $P_{c,d}$ for the b, c, d triplet to form a Laplace relation, which is not the case, see table 5. To continue the chain, planet b would have needed a period of ~ 1.95 d. Its current period of 1.91 d could indicate that it was previously in the chain but pulled away, possibly by tidal forces.

Figure 9 shows the evolution of the Laplace angles when integrating the nominal solution given in Tables 3 and 4, starting at the beginning of the observation of TESS sector 2. The three angles librate over the integrated time for the selected initial conditions, with combination of periods ranging from a few years to several decades. The exact periods and amplitudes of these variations depend on the masses and eccentricities of the involved planets. The long-term stability of this system is discussed in section 6.3, while the theoretical equilibria of the resonant angles are discussed in section 6.2.

6.2. Equilibria of the resonant chain

For a given resonant chain there might exist several equilibrium values around which the Laplace angles could librate (Delisle 2017). For instance, the four planets known to orbit Kepler-223 are observed to librate around one of the six possible equilibria predicted by theory (Mills et al. 2016; Delisle 2017).

We use the method described in Delisle (2017) to determine the position of the possible equilibria for the Laplace angles of TOI-178. The five external planets (c to g) orbiting TOI-178 are involved in a 2:4:6:9:12 resonant chain. All consecutive pair of planets in the chain are close to first order MMR (1:2, 2:3, 2:3, 3:4). Moreover, as in the Kepler-223 system, there are also strong interactions between non-consecutive planets. Indeed, planet e and planet g (which are non-consecutive) are also close to a 1:2 MMR. As explained in Delisle (2017), this breaks the symmetry of the equilibria (i.e. the equilibrium is not necessarily at 180 deg), and the position of the equilibria for the Laplace angles depend on the planets' masses.

We solved for the position of these equilibria using the masses given in Tables 3 and 4. We also propagated the errors to estimate the uncertainty on the Laplace angles equilibria. We find two possible equilibria for the system, which are symmetric from each other with respect to 0 deg. We provide the values of the Laplace angles corresponding to the first equilibrium in Table 6 (the second one is simply obtained by taking $\psi_j \rightarrow -\psi_j$ for each angle).

It should be noted that these values correspond to the position of the fixed point around which the system is expected to librate. Depending on the libration amplitude, the instantaneous values of the Laplace angles can significantly differ from the equilibrium. For instance, in the case of Kepler-223, the amplitude of libration could be determined and is about 15 deg for all Laplace angles (Mills et al. 2016). In Table 6, we observe that all instantaneous values of Laplace angles (as of August 2018) are also found within 15 deg around the expected equilibrium. We note that, during the two years of observations, ψ_1 was moving away from the equilibrium (see the averaged derivatives in Table 6). This would imply a final (as of September 2020) distance from equilibrium of about 23 deg. On the other hand, ψ_2 was getting closer to the equilibrium and ψ_3 was only slowly evolving during this two years span. A more precise determination of the evolution of Laplace angles (with more data, and the detection of TTVs) would be needed to estimate the amplitude of libration of each angle. However, it is unlikely to find values so close to the equilibrium for each of the three angles just by chance. Therefore, these results provide a strong evidence that the system is indeed librating around the Laplace equilibrium.

6.3. Stability

The planets c to g are embedded in a resonant chain, which seems to greatly stabilize this planetary system.

The distance between the planets being quite small, their eccentricities may become a major source of instability. This point is illustrated by figure 10, which shows a section of the system's phase space. The initial conditions and masses of the planets are those displayed in Tables 3

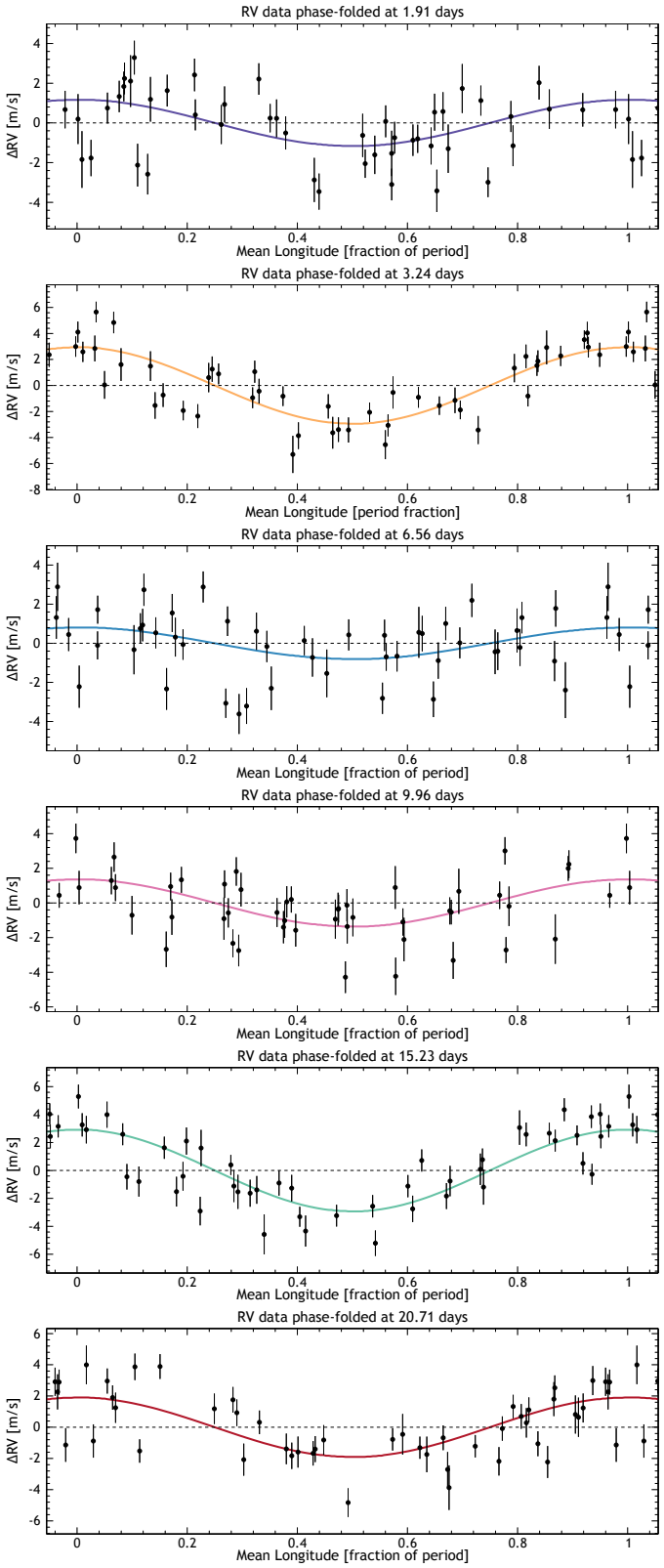

Fig. 8: Phase-folded RV. Error bars correspond to nominal errors.

and 4 except that of the planet f, for which the initial period and eccentricity vary, while all other planets start on circular orbits. The color code corresponds to a stability index based on the diffusion of the main frequencies of the

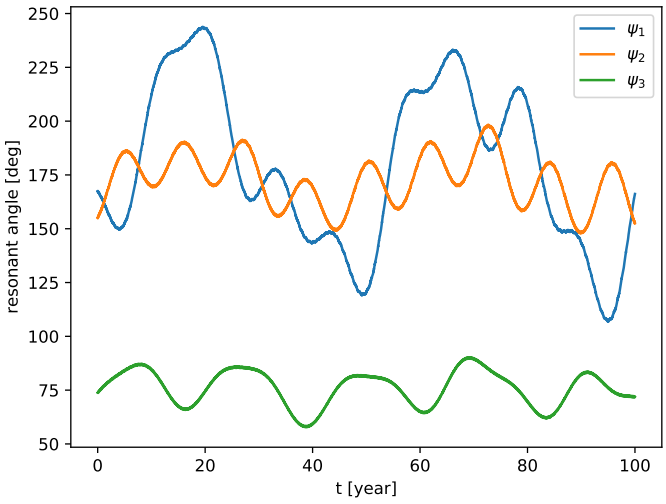

Fig. 9: Example of the evolution of the Laplace angles over 100 years, starting from TESS observation of sector 2, using the masses and orbital parameters from Tables 3 and 4

system defined as (Laskar 1990, 1993):

$$\log 10 \left| n_f^{(1)} - n_f^{(2)} \right| , \tag{3}$$

where $n_f^{(1)}$ and $n_f^{(2)}$ are the proper mean motion of planet f computed over the first half and the second half of the integration, respectively, implying that the stability increases from red to black (for more details see section 4.1 of Petit et al. 2018). This map shows that the eccentricity of planet f must not exceed a few hundredths for the system to remain stable. The same stability maps (not reproduced here), made for each of the planets of the system, lead to the same result: the planetary eccentricities have to be small in order to guaranty the system's stability. This constrain is verified if the system start with sufficiently small eccentricities. In particular, we verified that starting a set of numerical integration on circular orbit with masses and initial conditions close to the nominal one, and integrating the system over 100 000 years (i.e. about 19 million orbits of the planet b or 1.3 million orbits of planet g), do not excite the eccentricities above one hundredth in most cases.

All the stability maps P_i vs e_i, like the top panel of Fig. 10, show long quasi-vertical structures containing very stable regions in their central part and less stable regions at their edges. These are mainly mean-motion resonances between two or three planets. In particular, the blue area crossed by the white dashed line in the top panel of Fig. 10 corresponds to the resonant chain where the nominal system is located.

The bottom panel of Fig. 10 shows a different section of the phase space where P_f and P_g vary while all eccentricities are initialised at 0. This reveals part of the resonant structure of the system. The blue regions are stable while the green to red areas mark the instability caused by the resonance web. This figure still highlights the stability island in which the planetary system is located. This narrow region is surrounded by resonances: the $n_e - 3n_f + 2n_g = 0$ Laplace resonance (central diagonal strip), high order 2-body MMRs between planet f and g (horizontal strips); high order 2-body MMRs between planet e and f (vertical lines).

The extent of this resonant chain versus planet f initial period and mass is shown in Fig. 11. On both panels, the X-axis corresponds to the orbital period of planet f, while the Y-axis corresponds to the planetary mass. The figure presents two different, but complementary, aspects of the dynamics of TOI-178. The bottom panel indicates whether the Laplace angles ψ_1, ψ_2 and ψ_3 librate or not. More precisely, the color code corresponds to the number of angles that librate during the first 200 years of integration. The top panel present a stability index based on diffusion in main frequencies. Three regions stand out clearly from this figure, each with a different dynamical regime.

The central region (yellow on the bottom panel) where the three Laplace angles librate simultaneously (see also Fig.9) shows the heart of the 2:4:6:9:12 resonant chain, where the nominal system is located. On the stability map (top), its dark blue color reveals a very low diffusion rate and therefore a very long-term stability. This central region seems not to dependent strongly on the mass of planet f.

On the other hand, the modification of the orbital period has many more consequences. Indeed, outside of the central region where the three Laplace angles librates, which is about 0.015 days wide, chaotic layers are present (red on top panel panel, dark-blue on bottom) where none of three Laplace angles librate. Here, the red color of the stability index corresponds to a significant, but moderate diffusion rate. Thus, although in this region the trajectories are not quasiperiodic, the chaos has limited consequences (it is bounded) and does probably not lead to the destruction of the system.

Outside of these layers lies a very stable (quasiperiodic) region. The blue on the Laplace angle map shows that only one Laplace angle librates while the others circulate. Although the 2:4:6:9:12 chain is broken, the planets c, d, e, g remain inside the 2:4:6:12 resonant chain, independently of planet f orbital period. This demonstrates the robustness of these resonances. The stability map indicates a very strong regularity of the whole region. Nevertheless, one can notice the presence of some narrow zones where the diffusion is more important induced by high order orbital resonances, but without any significant consequence on the stability of the system.

Although the study described in this section gives only a very partial picture of the structure of the phase space (parameter space) of the problem, it can be seen that as long as the system is in the complete resonance chain, which is the case for the nominal derived parameters and for the bulk of the posterior given in Tables 3 and 4, it remains stable.

6.4. Expected TTVs

Since planets c, d, e, f and g are pairwise close to first order MMRs, we expect TTVs to occur over the super-period (Eq.1, see also Lithwick et al. 2012), which is roughly 260 days for all these pairs (Table 5). The amplitude of these TTVs depends on the masses and eccentricities of each planet involved in the pair. Since the stability analysis concludes that the system is more stable with eccentricities close to 0, we integrate the initial conditions described in Tables 3 and 4 over 6 years, starting during the observation of TESS sector 2 using the `rebound` package (Rein & Liu 2012). The resulting TTVs are shown in Fig.12.

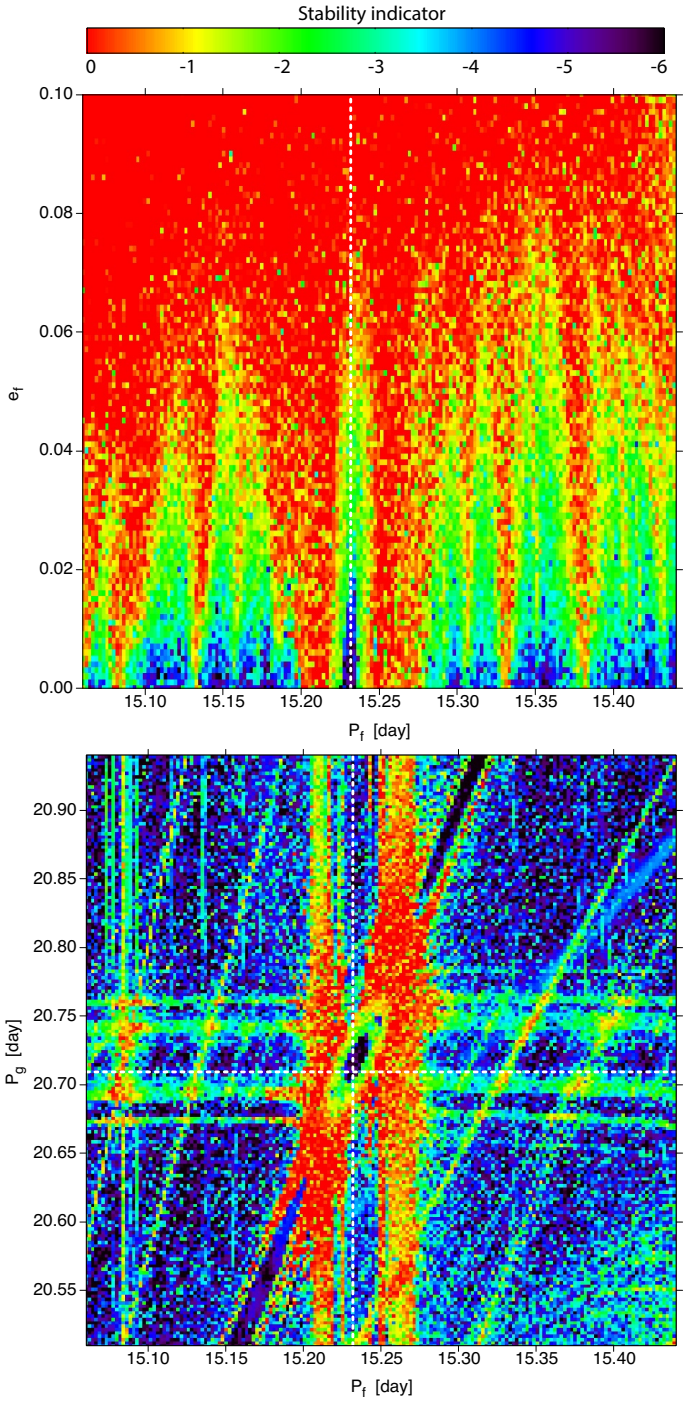

Fig. 10: Stability indicator (defined in eq. 3) for TOI-178 as a function of the periods and eccentricity of planet f (*top*), red shows the initial conditions of unstable trajectories, while blue shows stable (quasi-periodic) trajectories. The *bottom* panel shows the same stability criterion as with respect to the initial periods of planets f and g . The white dashed lines show the observed periods reported in Table 4.

In addition to the terms coming from the super-periods, the 6 years evolution of the TTVs shows the hints of the long term evolution of the Laplace angles. As the exact shapes of the TTVs depends mainly on the masses of the involved planets, a yearly monitoring of the outer planets

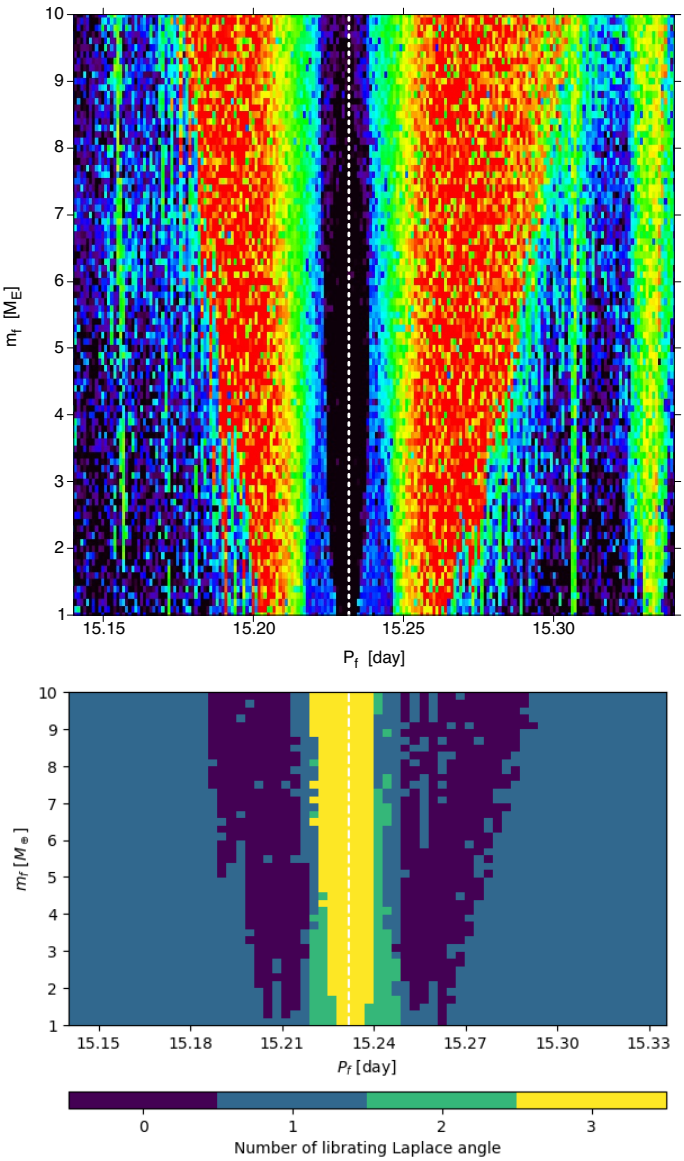

Fig. 11: Stability indicator as in Fig. 10 (*top*), and number of librating Laplace angles (*bottom*) for TOI-178 as a function of the period and mass of planet f. The white dashed line shows the observed period of planet f reported in Table 4.

can bring precise constrains on the orbital configuration and masses of this system. The detailed study of the TTVs of this system will be the object of a forthcoming paper.

7. Internal structure

7.1. Minimum mass of the protoplanetary disk

The total mass of the planets detected in TOI-178 ranges from $17.37 M_\oplus$ to $29.76 M_\oplus$. Assuming a mass fraction of H and He of maximum $\sim 20\%$ (similar to the ones of Uranus and Neptune), the amount of heavy elements in the planets is at least $13.8 M_\oplus$. This number can be compared with the mass of heavy elements one would expect in a protoplanetary disk that would be similar to the Minimum Mass Solar Nebula, but around TOI-178. Assuming a disk mass equal to 1% of the stellar mass, and using the metallicity of TOI-178 ($[Fe/H] = 0.0061$), the mass of heavy elements in such a disk would be equal to $\sim 13 M_\oplus$, which is remarkably similar to the minimum mass of heavy elements in planets, as mentioned above. The concept of MMSN, scaled appropriately to reflect the reduced mass and metallicity of TOI-178, seems therefore to be as applicable for this system as for the Solar System. Another implication of this comparison is that some problem in term of available mass would appear, should the planetary masses be revised to higher values or should another massive planet be detected in the same system. In such a case, the TOI-178 system would point towards a formation channel similar to the one envisioned for the Trappist-1 system (Schoonenberg et al. 2019).

7.2. Mass-radius relation

The six planets we detected in the TOI-178 system are in the super-Earth to mini-Neptune range, with radii ranging from 1.177 ± -0.074 to 2.91 ± 0.11 $R_\oplus$. Although the mass determination is limited by the extent of the available spectroscopic dataset, planet b and c appear to have roughly terrestrial density $0.93^{+0.29}_{-0.33}\rho_\oplus$ and $0.95^{+0.18}_{-0.21}\rho_\oplus$, respectively, $\rho_\oplus$ being the density of the Earth. The outer planets seem to have a density significantly lower, in particular, we estimate the density of planet d to be $0.16^{+0.04}_{-0.05}\rho_\oplus$.

Fig. 13 shows the position of the six planets in a mass-radius diagram, in comparison with planets with mass and radius uncertainties less than 40% (light gray). Planets belonging to four systems in Laplace resonance are indicated on the same diagram: Trappist-1, Kepler-60, Kepler-80 and Kepler 223. The diversity of planetary composition in TOI-178 is clearly visible on the diagram, with the two inner planets having a radius compatible with a gas-free structure, whereas the others contain water and/or gas. This is similar to the Kepler-80 system, where the two innermost planets are compatible with a gas-free structure, and the two outermost ones likely contain gas. Planets in the Kepler-223, Kepler-60 and Trappist-1 seem to have a more homogeneous structure, with all planets having a gas envelope in Kepler-223, and planets having a small gas envelope in Kepler-60 and Trappist-1.

Considering in more details the TOI-178 system, planets d,e and g are located above the pure water line, they for sure contain a non-zero gas mass fraction. Planets d and, depending on its mass, planet g, are located in a part of the diagram where no other planets exist (at least no planets with mass uncertainties smaller than 40 %) and must contain a large gas fraction.

Fig. 14 shows the location of the TOI-178 planets in a stellar isolation versus planetary radius diagram. The color code illustrates the density of exoplanets. This diagrams clearly shows the so-called 'evaporation valley'[4]. Planets b and c are located below the valley, and their high density could result from the evaporation of a primordial envelope. The outer planets are located above the valley, and have probably preserved (part of) their primordial gas envelope. The present day architecture of the TOI-178 system can therefore be emphasized considering the densities of planets

[4] Note that if the presence of a valley seems robust, it could be due to effect that are not related to evaporation, e.g. core cooling (Gupta & Schlichting 2019) or from combined formation and evolution effects (Venturini et al. 2020).

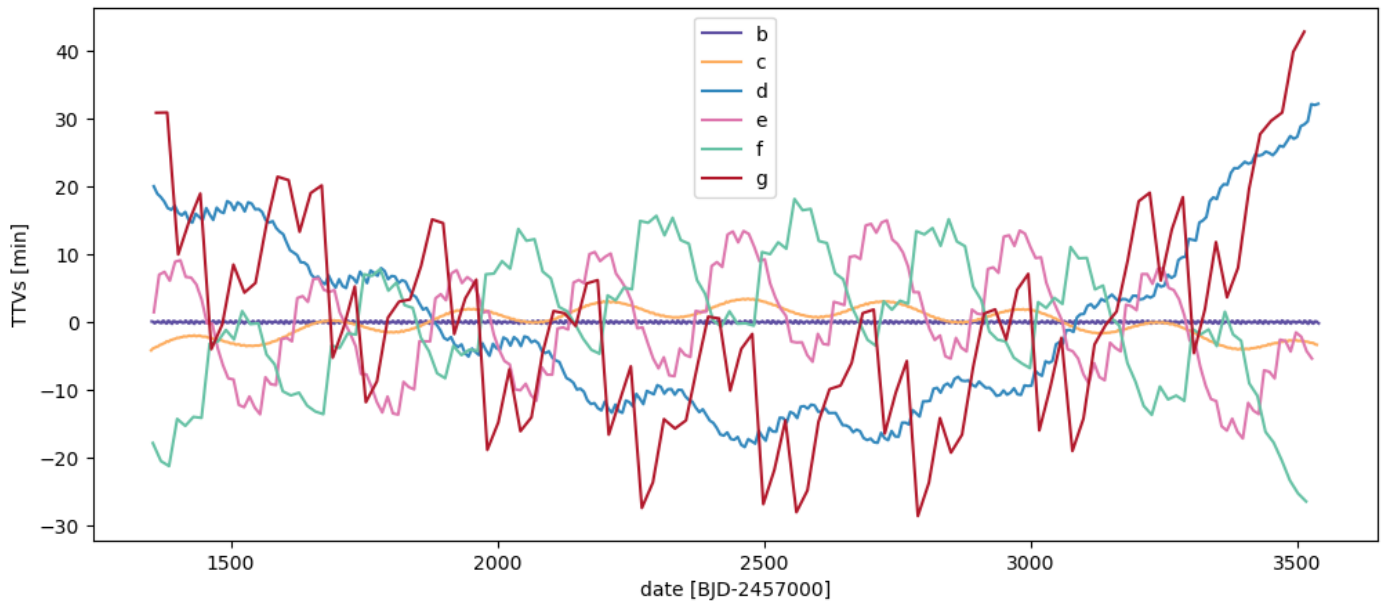

Fig. 12: Example of TTVs of the 6 planets of TOI-178, starting from TESS observation of Sector 2 and spanning 6 years, using the masses and orbital parameters from Tables 3 and 4.

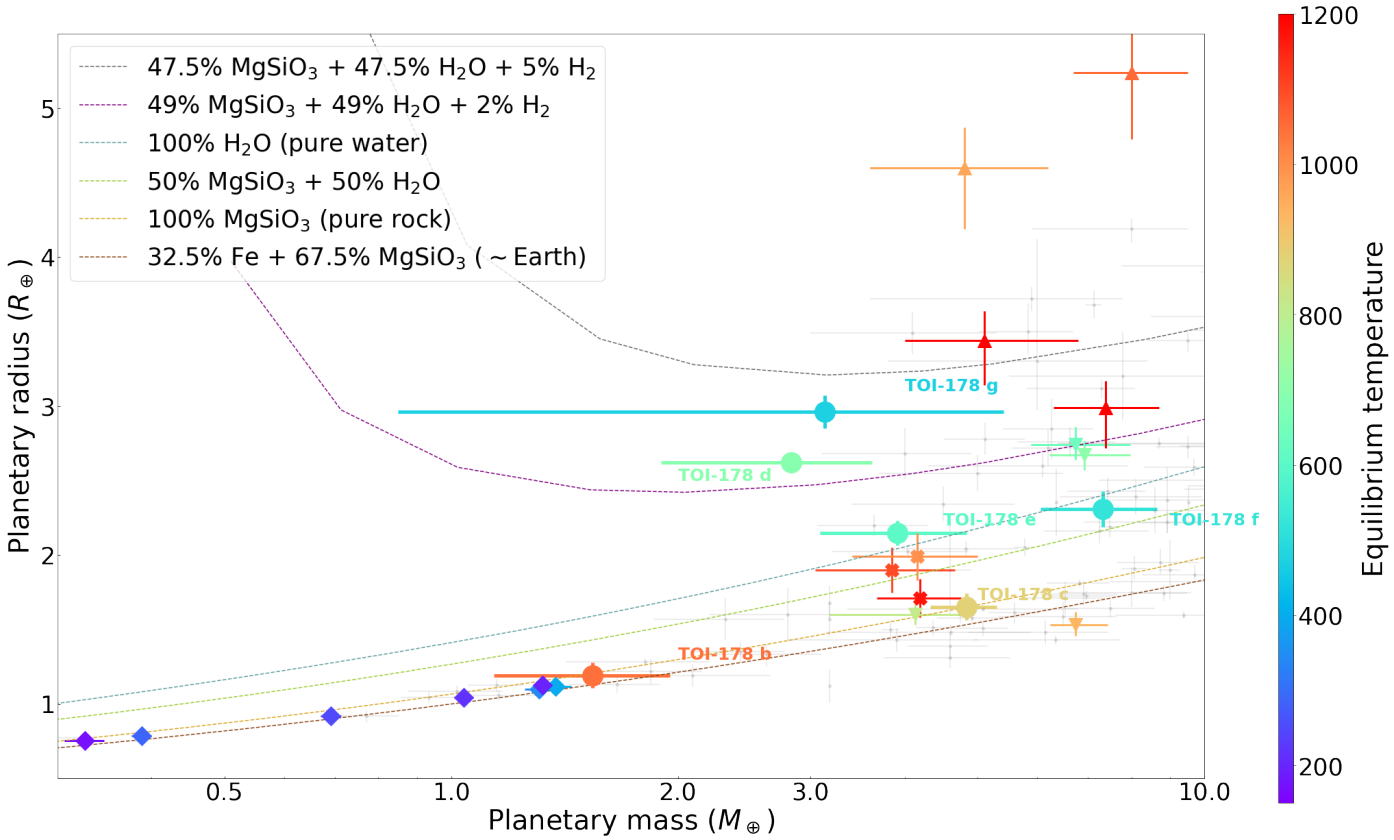

Fig. 13: The TOI-178 planets compared to other known transiting exoplanets with radius and mass uncertainties less than 40% (grey), and other system known to harbour a Laplace resonance. Data on known exoplanets were taken from NASA Exoplanet Archive on 18 September 2020. The dashed lines show theoretical mass-radius curves for some idealized compositionsZeng et al. (2019). The six planets orbiting around TOI-178 are indicated, the color of the points and error bars giving the equilibrium temperature. The seven planets orbiting Trappist-1 are shown with diamonds, the parameters being taken from Agol et al. (2020). The three planets orbiting Kepler-60 are shown with X, the parameters are taken from Jontof-Hutter et al. (2016). The four planets orbiting Kepler-80 are shown with bottom pointing triangles, the parameters being taken from MacDonald et al. (2016). The four planets orbiting Kepler-223 are shown with up pointing triangles, the parameters being taken from Mills et al. (2016).

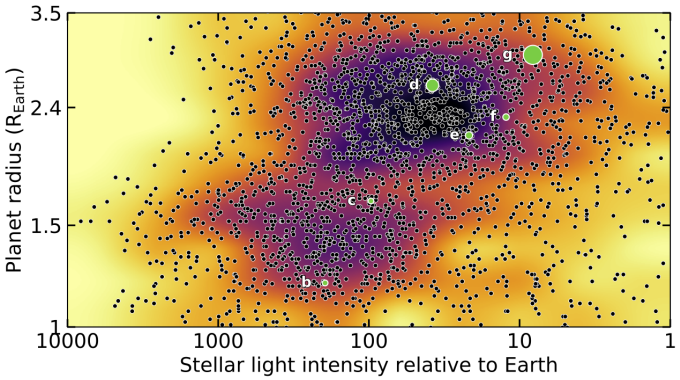

Fig. 14: Position of the TOI-178 planets in a stellar light intensity (relative to Earth) *versus* planetary radius diagram. The marker size is inversely proportional to the density and the color-code gives the density of exoplanets, from yellow for empty regions of the diagram to violet for high-density / highly populated regions.

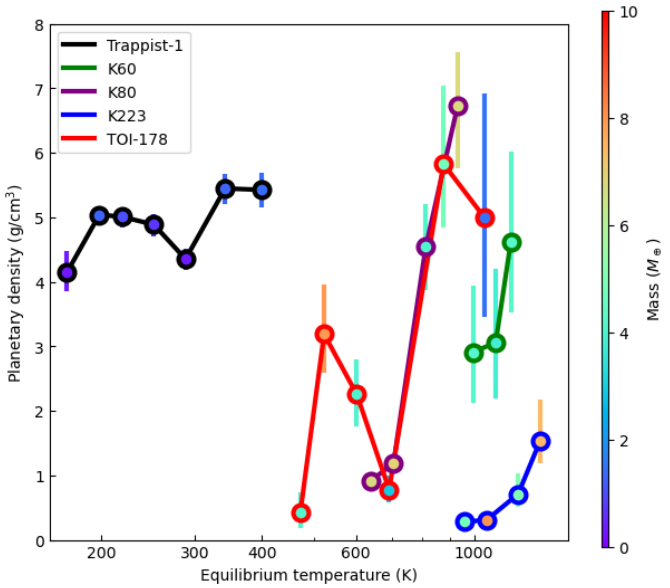

Fig. 15: Densities of planets in the TO-178, Trappist-1, Kepler-60, Kepler-80 and Kepler-223 systems, as a function of their equilibrium temperature. The error bars give the 16% and 84% quantile and the marker is located at the median of the computed distribution. The color code gives the planetary mass in Earth masses. The parameters of the planets are taken from the references mentioned in Fig. 13.

which is known to results from combined formation and evaporation processes.

7.3. Comparison with other systems in Laplace resonance

The difference between the TOI-178 system and other systems in Laplace resonance can clearly be seen on Fig. 15 where we show the density of planets as a function of their equilibrium temperature for the same systems as in Fig. 13. In Kepler-60, Kepler-80 and Kepler-223, the density of planets is decreasing when the equilibrium temperature decreases. This can be understood as the effect of evaporation that removes part of the primordial gaseous envelope, this effect being stronger for planets closer to their star. In Trappist-1, the density of planets is always higher than 4 g/cm^3, and increasing (with the exception of Trappist-1 f) when decreasing the equilibrium temperature. This is likely to result from the presence of more ices in planets far from the star (Agol et al. 2020). In the TOI-178 system, the density of planets is not a growing function of the equilibrium temperature, as for the three Kepler systems. Indeed, TOI-178f has a density higher than planets e , and TOI-178d has a density smaller than planet e.

Planet f is substantially more massive than all the other planets in the system. From a formation perspective, one would expect that this planet should have a density smaller than the other planets, in particular planet e, at the end of the formation phase, as we can observe for example for Jupiter, Saturn, Uranus and Neptune. Since this planet is further away from the star compared to planet e, evaporation should have been less effective for planet f compared to planet e. The combined effect of formation and evolution should therefore lead to a smaller density for planet f compared to planet e. Similarly, planet d is smaller than planet e and located closer to the star. Using the same arguments, the combined effect of formation and evolution should have led to planet d having a density larger than planet e. The TOI-178 system seems therefore at odd with the general understanding of planetary formation and evaporation where one would expect the density to decrease when the distance to the star increase, or when the mass of the planet increase.

7.4. Internal structure modeling

We have used a Bayesian analysis in order to compute the posterior distribution of the planetary internal structure parameters. The method we use follows closely the one of Dorn et al. (2015) and Dorn et al. (2017), and has already been used in Mortier et al. (2020) and Delrez (2020 - *submitted*). We here recall the main physical assumptions of the model.

The model is split in two parts, the first is the forward model, which provide the planetary radius as a function of the internal structure parameters, the second is the Bayesian analysis which provide the posterior distribution of the internal structure parameters, given the observed radii, masses, and stellar parameters (in particular its composition).

For the forward model, we assume that each planet is made of four layers: an iron/sulfur inner core, a mantle, a water layer and a gas layer. We use for the core the Equation of State (EOS) of Hakim et al. (2018), for the silicate mantle, the EOS of Sotin et al. (2007), and the water EOS is taken from Haldemann et al. (2020). These three layers constitute the 'solid' part of the planets. The thickness of the gas layer (assumed to be made of pure H/He) is computed as a function of the stellar age, mass and radius of the solid part, and irradiation from the star, using the formulas of Lopez & Fortney (2014). The internal structure parameters of each planet are therefore the iron molar fraction in the core, the Si and Mg molar fraction in the mantle, the mass fraction of all layers (inner core, mantle, water), the age of the planet (equal to the age of the star) and the irradiation from the star. More technical details on the calculation of the forward model are given in Appendix D.

In the Bayesian analysis part of model, we proceed in two steps. We first generate 150000 synthetic stars, their mass, radius, effective temperature, and age being taken at random following the stellar parameters computed in Sect. 3. The Fe/Si/Mg bulk molar ratio in the star are assumed to be solar, with an uncertainty of 0.05 (uncertainty on [Fe/H], see 3). For each of these stars, we generate 1000 planetary systems, varying the internal structure parameters of all planets, and assuming that the bulk Fe/Si/Mg molar ratios are equal to the stellar ones. We then compute the transit depth and RV semi-amplitude for each of the planets, and retain models that fit the observed data within the error bars. By doing so, we include the fact that all synthetic planets orbit a star with exactly the same parameters. Indeed, planetary masses and radii are correlated by the fact that the fitted quantities are the transit depth and RV semi-amplitude, which depend on the stellar radius and mass. In order to take into account this correlation, it is therefore important to fit the planetary system at once, and not each planet independently.

For the Bayesian analysis, we assume the following priors: the mass fraction of the gas envelop is assumed to be uniform in log. For the solid part, the mass fraction of the inner core, mantle and water layer are uniform on the simplex (the surface on which they add up to one). We assume in addition that the mas fraction of water is smaller than 50 % (Thiabaud et al. 2014; Marboeuf et al. 2014). The molar fraction of iron in the inner core is uniform between 0.5 and 1, and the molar fraction of Si, Mg and Fe in the mantle is uniform on the simplex (they also add up to one). In order to compare TOI-178 with other systems with a Laplace resonance, we have also done a Bayesian analysis for the Kepler-60, Kepler-80 and Kepler-223 systems in order to compute the probability distribution of the gas mass in the different planets. The parameters for all systems are taken from the references mentioned above, and for all systems we have assumed that [Si/H]=[Mg/H]=[Fe/H]. We have not considered the Trappist-1 system in this comparison, as it is likely that the variations in density in these planets results from variation in their ice content (Agol et al. 2020).

The posteriors distributions of the most important parameters (mass fractions, composition of the mantle) of each planets in TOI-178 are shown in Appendix D, Fig. D.2 to D.7. We focus here on the mass of gas in each of the planet, and plot in Fig. 16 the mass of the gaseous envelop for each planet as a function of their equilibrium temperature.

As can be seen on Fig. 16, the gas mass in planets generally decreases when the equilibrium temperature decreases in all three Kepler systems. One exception to this tendency is mass of Kepler-223d's envelope which is larger than the one of planet e in the same system. Kepler-223d is however more massive than planets c and e in the same system, and one expect from formation models that the mass of the primordial gas envelope is a growing function of the total planetary mass. In the case of TOI-178, the mass of gas globally also increases when the equilibrium temperature decrease, with the notable exception of planet d. Indeed, a linear interpolation would provide for planet d a gas mass of the order of $10^{-6}-10^{-5} M_\oplus$ whereas the interior structure modelling gives a value of $9.66 \times 10^{-3} M_\oplus$ and $2.56 \times 10^{-2} M_\oplus$ for the 16% and 84% quantiles. Even more intriguing, our results show that the amount of gas in planet d is larger than in planet e, this latter being both more massive and

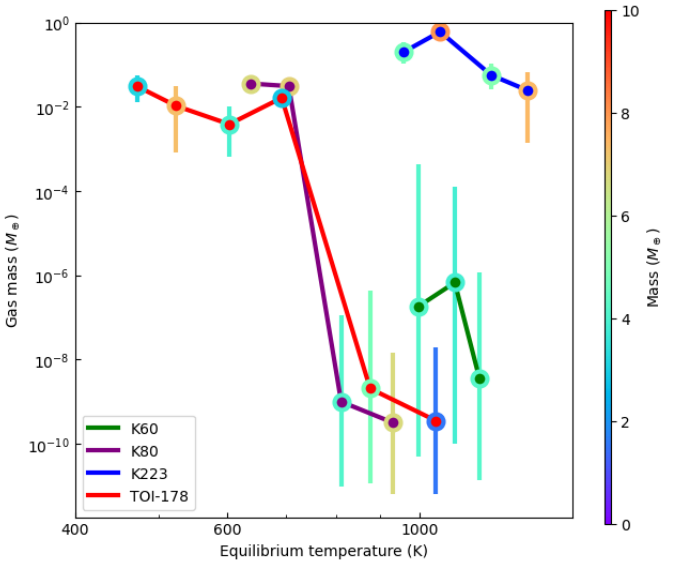

Fig. 16: Gas mass in the planets of the TOI-178, Kepler-60, Kepler-80 and Kepler-223 systems, as a function of their equilibrium temperature. The error bars give the 16% and 84% quantile and the marker is located at the median of the computed distribution. The color code gives the planetary mass in Earth masses.The parameters of the planets are taken from the references mentioned in Fig. 13.

at larger distance from the star. Indeed, from the joint probability distribution of all planetary parameters as provided by the Bayesian model, the probability that planet d has more gas than planet e is equal to 92%.

From a formation point of view, one generally expect that the mass of gas is a growing function of the core mass. From an evolution perspective, one also expect that evaporation should be more effective for planets closer to the star. Both would point towards a gas mass in planet d than should be smaller than the one in planet e. The large amount of gas in planet d, and more generally the apparent irregularity in the planetary envelope masses, is surprising in view of the apparent regularity of the orbital configuration of the system that was presented in Sect. 6.

8. Discussion and conclusions

In this study we presented new observations of TOI-178 by CHEOPS, ESPRESSO, NGTS and SPECULOOS. Thanks to this follow-up effort we were able to solve the architecture of the system: out of the three previously announced candidates at 6.56 d, 9.96 d and 10.3 d, we confirm the first two (6.56 d and 9.96 d) and re-attribute the transits of the third to 15.23 d and 20.7 d planets, in addition to the detection of two new inner planets at 1.91 d and 3.24 d, all of these planets were confirmed by follow-up observations. In total, we hence announce six planets in the super-Earth to mini-Neptune range, with orbital periods from 1.9 d to 20.7 d, all of them but the innermost in a 2:4:6:9:12 Laplace resonances chain. Current ephemerides and mass estimations indicate a very stable system, with Laplace angles librating over decades.

As there is no theoretical reason for the resonant chain to stop at 20.7 days, and the current limit probably comes from the duration of the available photometric and

Table 7: Potential periods that would continue the resonant chain in a near $(k+q) : k$ MMR with planet g, taking the super-period at 260 days, see equations in Appendix C. Changing the super-period by a few days typically change the resulting period by less than 0.1 day.

k, q	Period [day]
1, 1	45.0028
2, 1	32.3522
3, 1	28.3653
4, 1	26.4124
5, 1	25.2533
3, 2	36.4508
5, 2	29.9470
7, 2	27.2461

radial velocity datasets, we give in table 7 the periods that continue the resonant chain for first ($q = 1$) and second order ($q = 2$) MMRs. These periods result from the equations detailed in Appendix C. In the TOI-178 system, as well as in similar systems in Laplace resonance, planet pairs are nearly all near first order MMRs. The most likely of the periods shown in table 7 are therefore the first order solutions with low k hence 45.00, 32.35, or 28.36 days. We note that, for a star like TOI-178, the inner boundary of the habitable zone lies around 0.2 AU, or at a period of the order of 40 days. Additional planets in the Laplace resonance could therefore orbit inside, or very close to, the habitable zone.

The brightness of TOI-178 allows for further characterisation of the system both by photometric measurements, radial velocities and transit spectroscopy. These measurements will be essential to further constrain the system, not only on its orbital architecture, but also for the physical characterisation of the different planets.

As discussed above, the current mass and radii determinations show significant differences between the compositions of the different planets. It appears that the two innermost planets are likely to be rocky, which may be due to the fact that they have lost their primary, hydrogen-dominated atmospheres through escape (Kubyshkina et al. 2018, 2019), whereas all the other planets may have retained part of their primordial gas envelope. In this respect, the different planets of the TOI-178 system lie on both sides of the radius valley (Fulton et al. 2017). Therefore, reconstructing the past orbital and atmospheric history of this planet may provide clues regarding the origin of the valley. The system is located at a declination in the sky that makes it observable by most ground-based observatories around the globe. Furthermore, the host star is bright enough and the radii of the outer planets large enough to make them possibly amenable to optical and infrared transmission spectroscopy observations from both ground and space, particularly by employing the upcoming E-ELT and JWST facilities. Indeed, it has been shown that the James Webb Space Telescope has the capacity to perform transmission spectroscopy of planets with radii down to 1.5 $R_\oplus$ (Samuel et al. 2014).

The two planets d and f are particularly interesting as their density if very different from the ones of their neighbors, and as they depart from the general tendency of planetary density decreasing for decreasing equilibrium temperatures. The densities of planest d and f, in the context of the general trend seen in TOI-178, is difficult to understand in term of formation and evaporation process, and could be difficult to reproduce by planetary system formation models (Mordasini et al. 2012; Alibert et al. 2013; Emsenhuber et al. 2020). We stress that, even though two different analyses yielded similar estimates of mass and densities, they are made with only forty-six data points. As such, these estimates need to be confirmed by further RV measurements, which would provide in particular a better frequency resolution and confirm the mass estimate of planet f.

We note finally that the orbital configuration of TOI-178 is too fragile to survive giant impacts, or even significant close encounters: Fig. 10 shows that sudden change of period of one of the planets of less than a few $\sim .01$ d can render the system chaotic, while Fig. 11 shows that modifying a single period axis can break the resonant structure of the entire chain. Understanding in a single framework the apparent dis-order in term of planetary density on one side, and the very high level of order seen in the orbital architecture on the other side will be represent a challenge for planetary system formation models. Additional observations with *CHEOPS* and RV facilities will allow further constraining the internal structure of all planets in the system, and in particular the (lack of) similarity between the water and gas mass fraction between planets.

In addition, TTVs are expected to be large in the TOI-178 system (see Fig. 12), and to occur on periods of years. Future observations of this system can be used to measure the planetary masses directly from TTVs, and compare the result with masses derived from RV measurements. This could provide a benchmark to assess the capability of mass measurement through TTVs.

Furthermore, the innermost planet, b, lies just outside the 3:5 MMR with planet c, albeit a bit too far to be part of the Laplace chain, which would require a period of $\sim$ 1.95d. Since the formation of the Laplace resonant chain probably result from a slow drift from a chain of two-planet resonances due to tidal effects (Papaloizou & Terquem 2010; Delisle et al. 2012; Papaloizou 2015; MacDonald et al. 2016), the current state of the system might constrain the dissipative processes that tore apart the innermost link of the chain, while the rest of the configuration survived.

The TOI-178 system as revealed by the recent observations described in this paper cumulates a number of very important features: Laplace resonances, variation in densities from planet to planet, stellar brightness that allows a number of follow-up observations (photometric, atmospheric, spectroscopic). It is therefore likely to become one of the Rosetta Stones to understand planet formation and evolution, even more so if additional planets continuing the chain of Laplace resonances would be discovered orbiting inside the habitable zone.

Software list:

– `allesfitter` (Günther & Daylan 2020).

- astropy.
- batman/
- `celerite` (Foreman-Mackey et al. 2017a).
- CHEOPS DRP (Hoyer et al. 2020).
- `CHEOPSim` (Futyan et al. 2020).
- `dynesty` (Speagle 2020; Skilling 2004, 2006a; Higson et al. 2019; Buchner 2014, 2017; Skilling 2006b).
- `ellc` (Maxted 2016).
- `emcee` (Foreman-Mackey et al. 2013).
- `ipython` (Pérez & Granger 2007).
- ℓ_1 periodogram (Hara et al. 2017)[5]
- `lmfit` (Newville et al. 2014).
- `matplotlib` (Hunter 2007).
- `numpy` (Harris et al. 2020).
- `pycheops`[6] Maxted et al., *in prep.*.
- rebound
- `seaborn`[7]
- `scipy` (Virtanen et al. 2020).
- `spleaf` (Delisle et al. 2020)[8]
- `tqdm` (da Costa-Luis et al. 2018).
- Tensorflow
- Keras

Acknowledgements. The authors acknowledge support from the Swiss NCCR PlanetS and the Swiss National Science Foundation. YA and MJH acknowledge the support of the Swiss National Fund under grant 200020_172746. ACC and TW acknowledge support from STFC consolidated grant number ST/M001296/1. This work was granted access to the HPC resources of MesoPSL financed by the Region Ile de France and the project Equip@Meso (reference ANR-10-EQPX-29-01) of the programme Investissements d'Avenir supervised by the Agence Nationale pour la Recherche. Based on data collected under the NGTS project at the ESO La Silla Paranal Observatory. The NGTS facility is operated by the consortium institutes with support from the UK Science and Technology Facilities Council (STFC) project ST/M001962/1. V.A. acknowledges the support from FCT through Investigador FCT contract nr. IF/00650/2015/CP1273/CT0001. We acknowledge support from the Spanish Ministry of Science and Innovation and the European Regional Development Fund through grants ESP2016-80435-C2-1-R, ESP2016-80435-C2-2-R, PGC2018-098153-B-C33, PGC2018-098153-B-C31, ESP2017-87676-C5-1-R, MDM-2017-0737 Unidad de Excelencia "María de Maeztu"- Centro de Astrobiología (INTA-CSIC), as well as the support of the Generalitat de Catalunya/CERCA programme. The MOC activities have been supported by the ESA contract No. 4000124370. S.C.C.B. acknowledges support from FCT through FCT contracts nr. IF/01312/2014/CP1215/CT0004. XB, SC, DG, MF and JL acknowledge their role as ESA-appointed CHEOPS science team members. ABr was supported by SNSA. A.C. acknowledges support by CFisUC projects (UIDB/04564/2020 and UIDP/04564/2020), ENGAGE SKA (POCI-01-0145-FEDER-022217), and PHOBOS (POCI-01-0145-FEDER-029932), funded by COMPETE 2020 and FCT, Portugal. The Belgian participation to CHEOPS has been supported by the Belgian Federal Science Policy Office (BELSPO) in the framework of the PRODEX Program, and by the University of Liège through an ARC grant for Concerted Research Actions financed by the Wallonia-Brussels Federation. This work was supported by FCT - Fundação para a Ciência e a Tecnologia through national funds and by FEDER through COMPETE2020 - Programa Operacional Competitividade e Internacionalização by these grants: UID/FIS/04434/2019; UIDB/04434/2020; UIDP/04434/2020; PTDC/FIS-AST/32113/2017 POCI-01-0145-FEDER- 032113; PTDC/FIS-AST/28953/2017 POCI-01-0145-FEDER-028953; PTDC/FIS-AST/28987/2017 POCI-01-0145-FEDER-028987. O.D.S.D. is supported in the form of work contract (DL 57/2016/CP1364/CT0004) funded by national funds through FCT. B.-O.D. acknowledges support from the Swiss National Science Foundation (PP00P2-163967). MF and CMP gratefully acknowledge the support of the Swedish National Space Agency (DNR 65/19, 174/18). DG gratefully acknowledges financial support from the CRT foundation under Grant No. 2018.2323 "Gaseousor rocky? Unveiling the nature of small worlds". EG gratefully acknowledges support from the David and Claudia Harding Foundation in the form of a Winton Exoplanet Fellowship. M.G. is an F.R.S.-FNRS Senior Research Associate. MNG ackowledges support from the MIT Kavli Institute as a Juan Carlos Torres Fellow. JH acknowledges the support of the Swiss National Fund under grant 200020_172746. JSJ acknowledges support by FONDECYT grant 1201371, and partial support from CONICYT project Basal AFB-170002. AJ acknowledges support from ANID – Millennium Science Initiative – ICN12_009 and from FONDECYT project 1171208. This work was also partially supported by a grant from the Simons Foundation (PI Queloz, grant number 327127). Acknowledges support from the Spanish Ministry of Science and Innovation and the European Regional Development Fund through grant PGC2018-098153-B- C33, as well as the support of the Generalitat de Catalunya/CERCA programme. S.G.S. acknowledge support from FCT through FCT contract nr. CEECIND/00826/2018 and POPH/FSE (EC). This research received funding from the MERAC foundation, from the European Research Council under the European Union's Horizon 2020 research and innovation programme (grant agreement nº 803193/ BEBOP, and from the Science and Technology Facilites Council (STFC, grant nº ST/S00193X/1). V.V.G. is an F.R.S-FNRS Research Associate. JIV acknowledges support of CONICYT-PFCHA/Doctorado Nacional-21191829. M. R. Z. O. acknowledges financial support from projects AYA2016-79425-C3-2-P and PID2019-109522GB-C51 from the Spanish Ministry of Science, Innovation and Universities. This work has made use of data from the European Space Agency (ESA) mission *Gaia* (`https://www.cosmos.esa.int/gaia`), processed by the *Gaia* Data Processing and Analysis Consortium (DPAC, `https://www.cosmos.esa.int/web/gaia/dpac/consortium`). Funding for the DPAC has been provided by national institutions, in particular the institutions participating in the *Gaia* Multilateral Agreement.

[5] https://github.com/nathanchara/l1periodogram
[6] https://github.com/pmaxted/pycheops
[7] https://seaborn.pydata.org/index.html
[8] https://gitlab.unige.ch/Jean-Baptiste.Delisle/spleaf

References

Agol, E., Dorn, C., Grimm, S. L., et al. 2020, arXiv e-prints, arXiv:2010.01074
Alibert, Y., Carron, F., Fortier, A., et al. 2013, A&A, 558, A109
Alibert, Y. & Venturini, J. 2019, A&A, 626, A21
Baluev, R. V. 2008, MNRAS, 385, 1279
Barbary, K. 2016, Journal of Open Source Software, 1, 58
Benz, W., Broeg, C., Fortier, A., et al. 2020, arXiv e-prints, arXiv:2009.11633
Bertin, E. & Arnouts, S. 1996, A&AS, 117, 393
Blackwell, D. E. & Shallis, M. J. 1977, MNRAS, 180, 177
Bryant, E. M., Bayliss, D., McCormac, J., et al. 2020, MNRAS, 494, 5872
Buchner, J. 2014, arXiv e-prints, arXiv:1407.5459
Buchner, J. 2017, arXiv e-prints, arXiv:1707.04476
Burdanov, A., Delrez, L., Gillon, M., & Jehin, E. 2018, in Handbook of Exoplanets, ISBN 978-3-319-55332-0. Springer International Publishing AG, part of Springer Nature, 2018, id.130, 130
Cabrera, J., Csizmadia, S., Erikson, A., Rauer, H., & Kirste, S. 2012, A&A, 548, A44
Castelli, F. & Kurucz, R. L. 2003, in IAU Symposium, Vol. 210, Modelling of Stellar Atmospheres, ed. N. Piskunov, W. W. Weiss, & D. F. Gray, A20
Chen, S. S., Donoho, D. L., & Saunders, M. A. 1998, SIAM JOURNAL ON SCIENTIFIC COMPUTING, 20, 33
Claret, A. & Bloemen, S. 2011, A&A, 529, A75
Correia, A. C. M., Delisle, J.-B., & Laskar, J. 2018, Planets in Mean-Motion Resonances and the System Around HD45364, ed. H. J. Deeg & J. A. Belmonte, 12
da Costa-Luis, C., L., S., Mary, H., et al. 2018
Dawson, R. I. & Fabrycky, D. C. 2010, ApJ, 722, 937
Delisle, J. B. 2017, A&A, 605, A96
Delisle, J. B., Hara, N., & Ségransan, D. 2020, A&A, 638, A95
Delisle, J.-B., Laskar, J., Correia, A. C. M., & Boué, G. 2012, Astron. Astrophys., 546, A71
Delisle, J. B., Ségransan, D., Dumusque, X., et al. 2018, A&A, 614, A133
Delrez, L., Gillon, M., Queloz, D., et al. 2018, in Society of Photo-Optical Instrumentation Engineers (SPIE) Conference Series, Vol. 10700, Proc. SPIE, 107001I
Dorn, C., Khan, A., Heng, K., et al. 2015, 577, A83
Dorn, C., Venturini, J., Khan, A., et al. 2017, 597, A37

Emsenhuber, A., Mordasini, C., Burn, R., et al. 2020, arXiv e-prints, arXiv:2007.05561
Fabrycky, D. C., Lissauer, J. J., Ragozzine, D., et al. 2014, ApJ, 790, 146
Foreman-Mackey, D., Agol, E., Ambikasaran, S., & Angus, R. 2017a, AJ, 154, 220
Foreman-Mackey, D., Agol, E., Ambikasaran, S., & Angus, R. 2017b, AJ, 154, 220
Foreman-Mackey, D., Hogg, D. W., Lang, D., & Goodman, J. 2013, PASP, 125, 306
Fulton, B. J., Petigura, E. A., Howard, A. W., et al. 2017, AJ, 154, 109
Futyan, D., Fortier, A., Beck, M., et al. 2020, A&A, 635, A23
Gaia Collaboration, Brown, A. G. A., Vallenari, A., et al. 2018, A&A, 616, A1
Gillon, M. 2018, Nature Astronomy, 2, 344
Gillon, M., Triaud, A. H. M. J., Demory, B.-O., et al. 2017, Nature, 542, 456
Goździewski, K., Migaszewski, C., Panichi, F., & Szuszkiewicz, E. 2016, MNRAS, 455, L104
Günther, M. N. & Daylan, T. 2020, arXiv e-prints, arXiv:2003.14371
Gupta, A. & Schlichting, H. E. 2019, MNRAS, 487, 24
Gustafsson, B., Edvardsson, B., Eriksson, K. and Jørgensen, U. G., Nordlund, Å., & Plez, B. 2008, A&A, 486, 951
Hakim, K., Rivoldini, A., Van Hoolst, T., et al. 2018, Icarus, 313, 61
Haldemann, J., Alibert, Y., Mordasini, C., & Benz, W. 2020, arXiv e-prints, arXiv:2009.10098
Hara, N. C., Bouchy, F., Stalport, M., et al. 2020, A&A, 636, L6
Hara, N. C., Boué, G., Laskar, J., & Correia, A. C. M. 2017, MNRAS, 464, 1220
Hara, N. C., Boué, G., Laskar, J., Delisle, J. B., & Unger, N. 2019, MNRAS, 489, 738
Harris, C. R., Millman, K. J., van der Walt, S. J., et al. 2020, Nature, 585, 357
Haywood, R. D., Collier Cameron, A., Queloz, D., et al. 2014, MNRAS, 443, 2517
Henrard, J. & Lemaitre, A. 1983, Celestial Mechanics, 30, 197
Higson, E., Handley, W., Hobson, M., & Lasenby, A. 2019, Statistics and Computing, 29, 891
Høg, E., Fabricius, C., Makarov, V. V., et al. 2000, A&A, 355, L27
Hoyer, S., Guterman, P., Demangeon, O., et al. 2020, A&A, 635, A24
Hunter, J. D. 2007, Computing in Science & Engineering, 9, 90
Irwin, M. J., Lewis, J., Hodgkin, S., et al. 2004, in Proc. SPIE, Vol. 5493, Optimizing Scientific Return for Astronomy through Information Technologies, ed. P. J. Quinn & A. Bridger, 411–422
Izidoro, A., Ogihara, M., Raymond, S. N., et al. 2017, MNRAS, 470, 1750
Jenkins, J. M., Twicken, J. D., McCauliff, S., et al. 2016, in Society of Photo-Optical Instrumentation Engineers (SPIE) Conference Series, Vol. 9913, Software and Cyberinfrastructure for Astronomy IV, 99133E
Jontof-Hutter, D., Ford, E. B., Rowe, J. F., et al. 2016, ApJ, 820, 39
Kipping, D. M. 2013, MNRAS, 435, 2152
Kovács, G., Zucker, S., & Mazeh, T. 2002, A&A, 391, 369
Kreidberg, L. 2015, PASP, 127, 1161
Kubyshkina, D., Cubillos, P. E., Fossati, L., et al. 2019, ApJ, 879, 26
Kubyshkina, D., Fossati, L., Erkaev, N. V., et al. 2018, A&A, 619, A151
Kurucz, R. L. 2013, ATLAS12: Opacity sampling model atmosphere program, Astrophysics Source Code Library
Laskar, J. 1990, Icarus, 88, 266
Laskar, J. 1993, Physica D: Nonlinear Phenomena, 67, 257
Lee, M. H. & Peale, S. J. 2002, ApJ, 567, 596
Leleu, A., Lillo-Box, J., Sestovic, M., et al. 2019, A&A, 624, A46
Leleu, A., Robutel, P., & Correia, A. C. M. 2015, Astron. Astrophys., 581, A128
Lendl, M., Csizmadia, S., Deline, A., et al. 2020, arXiv e-prints, arXiv:2009.13403
Lissauer, J. J., Fabrycky, D. C., Ford, E. B., et al. 2011, Nature, 470, 53
Lithwick, Y., Xie, J., & Wu, Y. 2012, ApJ, 761, 122
Lopez, E. D. & Fortney, J. J. 2014, 792, 1
Luger, R., Sestovic, M., Kruse, E., et al. 2017, ArXiv e-prints [arXiv:1703.04166]
MacDonald, M. G., Ragozzine, D., Fabrycky, D. C., et al. 2016, AJ, 152, 105
Marboeuf, U., Thiabaud, A., Alibert, Y., Cabral, N., & Benz, W. 2014, 570, A36
Marigo, P., Girardi, L., Bressan, A., et al. 2017, ApJ, 835, 77
Maxted, P. F. L. 2016, A&A, 591, A111
Mayor, M. & Queloz, D. 1995, Nature, 378, 355
McCormac, J., Pollacco, D., Skillen, I., et al. 2013, PASP, 125, 548
Mills, S. M., Fabrycky, D. C., Migaszewski, C., et al. 2016, Nature, 533, 509
Morbidelli, A. 2002, Modern celestial mechanics : aspects of solar system dynamics (Taylor & Francis, London, 2002, ISBN 0415279399)
Mordasini, C., Alibert, Y., Benz, W., Klahr, H., & Henning, T. 2012, A&A, 541, A97
Mortier, A., Zapatero Osorio, M. R., Malavolta, L., et al. 2020, arXiv e-prints, arXiv:2010.01993
Murray, C. A., Delrez, L., Pedersen, P. P., et al. 2020, Monthly Notices of the Royal Astronomical Society, 495, 2446, arXiv: 2005.02423
Newville, M., Stensitzki, T., Allen, D. B., & Ingargiola, A. 2014
Noyes, R. W. 1984, in Space Research in Stellar Activity and Variability, ed. A. Mangeney & F. Praderie, 113
Papaloizou, J. C. B. 2015, International Journal of Astrobiology, 14, 291
Papaloizou, J. C. B. & Terquem, C. 2010, MNRAS, 405, 573
Pepe, F., Cristiani, S., Rebolo, R., et al. 2020, arXiv e-prints, arXiv:2010.00316
Pérez, F. & Granger, B. E. 2007, Computing in Science & Engineering, 9
Petit, A. C., Laskar, J., & Boué, G. 2018, A&A, 617, A93
Piskunov, N. & Valenti, J. A. 2017, A&A, 597, A16
Pu, B. & Wu, Y. 2015, ApJ, 807, 44
Queloz, D., Henry, G. W., Sivan, J. P., et al. 2001, A&A, 379, 279
Rein, H. & Liu, S. F. 2012, A&A, 537, A128
Samuel, B., Leconte, J., Rouan, D., et al. 2014, A&A, 563, A103
Schoonenberg, D., Liu, B., Ormel, C. W., & Dorn, C. 2019, A&A, 627, A149
Scuflaire, R., Théado, S., Montalbán, J., et al. 2008, Ap&SS, 316, 83
Shapiro, S. S. & Wilk, M. B. 1965, Biometrika, 52, 591
Skilling, J. 2004, in American Institute of Physics Conference Series, Vol. 735, American Institute of Physics Conference Series, ed. R. Fischer, R. Preuss, & U. V. Toussaint, 395–405
Skilling, J. 2006a, Bayesian Anal., 1, 833
Skilling, J. 2006b, Bayesian Anal., 1, 833
Skrutskie, M. F., Cutri, R. M., Stiening, R., et al. 2006, AJ, 131, 1163
Smith, A. M. S., Eigmüller, P., Gurumoorthy, R., et al. 2020, Astronomische Nachrichten, 341, 273
Smith, J. C., Stumpe, M. C., Van Cleve, J. E., et al. 2012, PASP, 124, 1000
Sneden, C. 1973, Ph.D. Thesis, Univ. of Texas
Sotin, C., Grasset, O., & Mocquet, A. 2007, Icarus, 191, 337
Sousa, S. G. 2014, ARES + MOOG: A Practical Overview of an Equivalent Width (EW) Method to Derive Stellar Parameters, 297–310
Sousa, S. G., Santos, N. C., Adibekyan, V., Delgado-Mena, E., & Israelian, G. 2015, A&A, 577, A67
Speagle, J. S. 2020, MNRAS, 493, 3132
Stassun, K. G., Oelkers, R. J., Paegert, M., et al. 2019, AJ, 158, 138
Stassun, K. G., Oelkers, R. J., Pepper, J., et al. 2018, AJ, 156, 102
Stumpe, M. C., Smith, J. C., Catanzarite, J. H., et al. 2014, PASP, 126, 100
Terquem, C. & Papaloizou, J. C. B. 2007, ApJ, 654, 1110
Thiabaud, A., Marboeuf, U., Alibert, Y., et al. 2014, 562, A27
Valenti, J. A. & Piskunov, N. 1996, A&AS, 118, 595
Venturini, J., Guilera, O. M., Haldemann, J., Ronco, M. P., & Mordasini, C. 2020, arXiv e-prints, arXiv:2008.05513
Virtanen, P., Gommers, R., Oliphant, T. E., et al. 2020, Nature Methods, 17, 261
Wheatley, P. J., West, R. G., Goad, M. R., et al. 2018, MNRAS, 475, 4476
Wright, E. L., Eisenhardt, P. R. M., Mainzer, A. K., et al. 2010, AJ, 140, 1868
Yee, S. W., Petigura, E. A., & von Braun, K. 2017, ApJ, 836, 77
Zeng, L., Jacobsen, S. B., Sasselov, D. D., et al. 2019, Proceedings of the National Academy of Science, 116, 9723

[1] Observatoire Astronomique de l'Université de Genève, Chemin des Maillettes 51, Sauverny, CH-1290, Switzerland
[2] Physikalisches Institut, University of Bern, Gesellsschaftstrasse 6, 3012 Bern, Switzerland
[3] Centre for Exoplanet Science, SUPA School of Physics and Astronomy, University of St Andrews, North Haugh, St Andrews KY16 9SS, UK
[4] IMCCE, UMR8028 CNRS, Observatoire de Paris, PSL Univ.,

Sorbonne Univ., 77 av. Denfert-Rochereau, 75014 Paris, France
[5] Aix Marseille Univ, CNRS, CNES, LAM, Marseille, France
[6] Department of Physics, University of Warwick, Gibbet Hill Road, Coventry CV4 7AL, UK
[7] Centre for Exoplanets and Habitability, University of Warwick, Gibbet Hill Road, Coventry CV4 7AL, UK
[8] Astrobiology Research Unit, Université de Liège, Allée du 6 Août 19C, B-4000 Lige, Belgium
[9] Institute of Planetary Research, German Aerospace Center (DLR), Rutherfordstrasse 2, 12489 Berlin, Germany
[10] School of Physics and Astronomy, University of Leicester, Leicester LE1 7RH, UK
[11] Instituto de Astrofísica e Ciências do Espaço, Universidade do Porto, CAUP, Rua das Estrelas, 4150-762 Porto, Portugal
[12] Centro de Astrofísica da Universidade do Porto, Rua das Estrelas, 4150-762 Porto, Portugal
[13] Departamento de Física e Astronomia, Faculdade de Ciências, Universidade do Porto, Rua do Campo Alegre, 4169-007 Porto, Portugal
[14] Instituto de Astrofísica de Canarias, 38200 La Laguna, Tenerife, Spain
[15] Departamento de Astrofísica, Universidad de La Laguna, 38206 La Laguna, Tenerife, Spain
[16] Camino El Observatorio 1515, Las Condes, Santiago, Chile
[17] ETH Zürich, Institute for Particle Physics and Astrophysics
[18] Institut de Ciències de l'Espai (ICE, CSIC), Campus UAB, Can Magrans s/n, 08193 Bellaterra, Spain
[19] Institut d'Estudis Espacials de Catalunya (IEEC), 08034 Barcelona, Spain
[20] ESTEC, European Space Agency, 2201AZ, Noordwijk, NL
[21] Depto. de Astrofísica, Centro de Astrobiologia (CSIC-INTA), ESAC campus, 28692 Villanueva de la Cãda (Madrid), Spain
[22] Space Research Institute, Austrian Academy of Sciences, Schmiedlstrasse 6, A-8042 Graz, Austria
[23] Center for Space and Habitability, Gesellsschaftstrasse 6, 3012 Bern, Switzerland
[24] Université Grenoble Alpes, CNRS, IPAG, 38000 Grenoble, France
[25] Department of Astronomy, Stockholm University, AlbaNova University Center, 10691 Stockholm, Sweden
[26] Institute of Optical Sensor Systems, German Aerospace Center (DLR), Rutherfordstrasse 2, 12489 Berlin, Germany
[27] Department of Earth, Atmospheric and Planetary Science, Massachusetts Institute of Technology, 77 Massachusetts Avenue, Cambridge, MA 02139, USA
[28] Admatis, Miskok, Hungary
[29] Université de Paris, Institut de physique du globe de Paris, CNRS, F-75005 Paris, France
[30] CFisUC, Department of Physics, University of Coimbra, 3004-516 Coimbra, Portugal
[31] INAF - Osservatorio Astronomico di Trieste, via G. B. Tiepolo 11, I-34143 Trieste, Italy
[32] INAF - Osservatorio Astrofisico di Torino, via Osservatorio 20, 10025 Pino Torinese, Italy
[33] Lund Observatory, Dept. of Astronomy and Theoretical Physics, Lund University, Box 43, 22100 Lund, Sweden
[34] Astrobiology Research Unit, Université de Liège, Allée du 6 Août 19C, 4000 Liège, Belgium
[35] Space sciences, Technologies and Astrophysics Research (STAR) Institute, Université de Liège, Allée du 6 Août 19C, 4000 Liège, Belgium
[36] INAF, Istituto di Astrofisica e Planetologia Spaziali, via del Fosso del Cavaliere 100, 00133 Roma, Italy
[37] European Southern Observatory, Alonso de Coórdova 3107, Vitacura, Regioón Metropolitana, Chile
[38] Leiden Observatory, University of Leiden, PO Box 9513, 2300 RA Leiden, The Netherlands
[39] Department of Space, Earth and Environment, Chalmers University of Technology, Onsala Space Observatory, 43992 Onsala, Sweden
[40] Dipartimento di Fisica, Università degli Studi di Torino, via Pietro Giuria 1, I-10125, Torino, Italy
[41] Center for Astronomy and Astrophysics, Technical University Berlin, Hardenberstrasse 36, 10623 Berlin, Germany
[42] Astronomy Unit, Queen Mary University of London, Mile End Road, London E1 4NS, UK
[43] Cavendish Laboratory, JJ Thomson Avenue, Cambridge CB3 0HE, UK
[44] University of Vienna, Department of Astrophysics, Türkenschanzstrasse 17, 1180 Vienna, Austria
[45] Department of Physics and Kavli Institute for Astrophysics and Space Research, Massachusetts Institute of Technology, Cambridge, MA 02139, USA
[46] Space Sciences, Technologies and Astrophysics Research (STAR) Institute, Université de Liège, Allée du 6 Août 19C, B-4000 Liège, Belgium
[47] Departamento de Astronomía, Universidad de Chile, Camino El Observatorio 1515, Las Condes, Santiago, Chile
[48] Centro de Astrofísica y Tecnologías Afines (CATA), Casilla 36-D, Santiago, Chile
[49] Facultad de Ingeniería y Ciencias, Universidad Adolfo Ibáñez, Av. Diagonal las Torres 2640, Peñalolén, Santiago, Chile
[50] Millennium Institute for Astrophysics, Chile
[51] Konkoly Observatory, Research Centre for Astronomy and Earth Sciences, 1121 Budapest, Konkoly Thege Miklós út 15-17, Hungary
[52] Brorfelde Observatory, Observator Gyldenkernes Vej 7, DK-4340 Tølløse, Denmark
[53] DTU Space, National Space Institute, Technical University of Denmark, Elektrovej 327, DK-2800 Lyngby, Denmark
[54] Institut d'astrophysique de Paris, UMR7095 CNRS, Université Pierre & Marie Curie, 98bis blvd. Arago, 75014 Paris, France
[55] INAF, Osservatorio Astronomico di Padova, Vicolo dell'Osservatorio 5, 35122 Padova, Italy
[56] Astrophysics Group, Keele University, Staffordshire, ST5 5BG, United Kingdom
[57] Department of Physics, University of Warwick, Coventry, UK
[58] INAF - Osservatorio Astronomico di Palermo, Piazza del Parlamento 1, 90134, Palermo, Italy
[59] IFPU, Via Beirut 2, 34151 Grignano Trieste
[60] Instituto de Astronomía, Universidad Católica del Norte, Angamos 0610, Antofagasta, Chile
[61] Instituto de Astrofísica e Ciências do Espaço, Faculdade de Ciências da Universidade de Lisboa, Campo Grande, PT1749-016 Lisboa, Portugal
[62] Department of Astrophysics, University of Vienna, Tuerkenschanzstrasse 17, 1180 Vienna, Austria
[63] INAF, Osservatorio Astrofisico di Catania, Via S. Sofia 78, 95123 Catania, Italy
[64] Instituto de Astrofísica de Canarias, 38200 La Laguna, Tenerife, Spain
[65] Departamento de Astrofísica, Universidad de La Laguna, 38206 La Laguna, Tenerife, Spain
[66] Dipartimento di Fisica e Astronomia "Galileo Galilei", Università degli Studi di Padova, Vicolo dell'Osservatorio 3, 35122 Padova, Italy
[67] Space Science Data Center, ASI, via del Politecnico snc, 00133 Roma, Italy
[68] Department of Physics, University of Warwick, Gibbet Hill Road, Coventry CV4 7AL, United Kingdom
[69] Fundación G. Galilei – INAF (Telescopio Nazionale Galileo), Rambla J. A. Fernández Pérez 7, E-38712 Breña Baja, La Palma, Spain
[70] INAF - Osservatorio Astronomico di Brera, Via E. Bianchi 46, I-23807 Merate, Italy
[71] Institut für Geologische Wissenschaften, Freie Universität Berlin, 12249 Berlin, Germany
[72] Paris Observatory, LUTh UMR 8102, 92190 Meudon, France

[73] School of Physics Astronomy, University of Birmingham, Edgbaston, Birmingham B15 2TT, United Kingdom
[74] ELTE Eötvös Loránd University, Gothard Astrophysical Observatory, 9700 Szombathely, Szent Imre h. u. 112, Hungary
[75] MTA-ELTE Exoplanet Research Group, 9700 Szombathely, Szent Imre h. u. 112, Hungary
[76] INAF, Osservatorio Astronomico di Roma, via Frascati 33, 00078 Monte Porzio Catone, Roma, Italy
[77] Institute of Astronomy, University of Cambridge, Madingley Road, Cambridge, CB3 0HA, United Kingdom
[78] Centro de Astrobiología (CSIC-INTA), Crta. Ajalvir km 4, E-28850 Torrejón de Ardoz, Madrid, Spain

Appendix A: Inspection of the CHEOPS data

The four *CHEOPS* visits were automatically processed through the DRP with individual frames undergoing various calibrations and corrections, with aperture photometry subsequently conducted for four aperture radii as has been highlighted in Section 4.1.2 and covered in detailed in Hoyer et al. 2020. The produced light curves with, often referred to as "raw" in order to indicate no post-processing detrending has taken place, obtained with the DEFAULT aperture, for all runs in this study are shown in Figs. A.1. For the first, third, and fourth visits the standard data processing within the DRP was performed, however for the second run careful treatment of telegraphic pixels was needed.

In *CHEOPS* CCD there is a large number of hot pixels (see for example Fig. 3). Moreover, some normal pixels can change their behaviour to an abnormal state within the duration of a visit. For example, a pixel can become *hot* after a SAA crossing of the satellite. These pixels are called *telegraphic* due to their unstable response during the observations; and they can disturb the photometry if located inside the photometric aperture. To discard that the detected transit events in the light curves correspond to the effect of *telegraphic* pixels, the data frames were carefully inspected and compared versus the detection map of hot pixels delivered by the *CHEOPS* DRP (see details in Hoyer et al. 2020). By doing this, one *telegraphic* pixel was detected inside the DEFAULT aperture at the end of the second visit of TOI-178. The exact CCD location of this abnormal pixel is shown if Fig. 3. The effect of this pixel in the photometry is shown in the form of a jump in flux in the light curve of the visit (top panel, Fig. A.2) at BJD∼2 459 076.5. which corresponds to the flux increase of the pixel (middle panel, Fig. A.2). After correcting the data, by simply cancelling the flux of this pixel through the full observation, and repeating the photometry extraction with the same aperture (R=25″) we removed the flux jump in the light curve (bottom panel, Fig. A.2). No telegraphic pixels were detected on the rest of the visits of TOI-178.

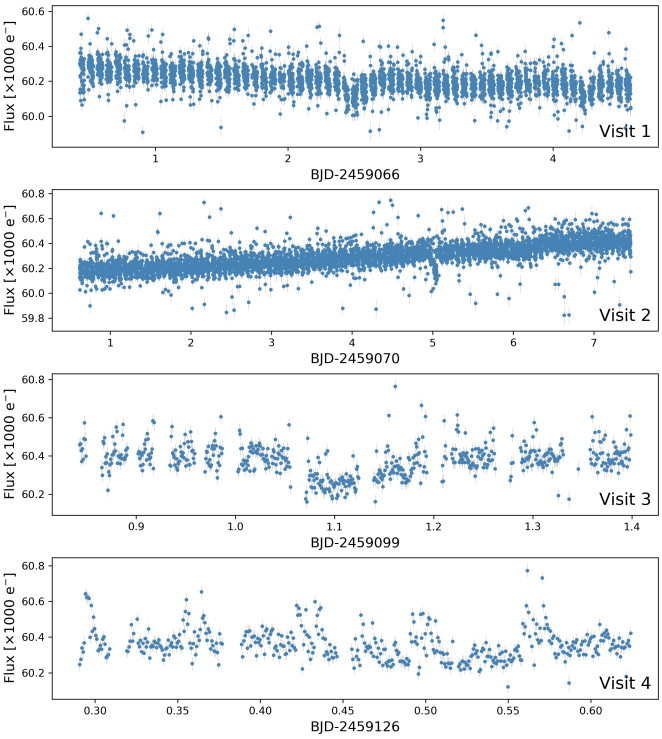

Fig. A.1: The DRP produced light curves (DEFAULT aperture) of the 4 *CHEOPS* visits of TOI-178 presented in this work. 3-σ outliers have been removed for better visualization.

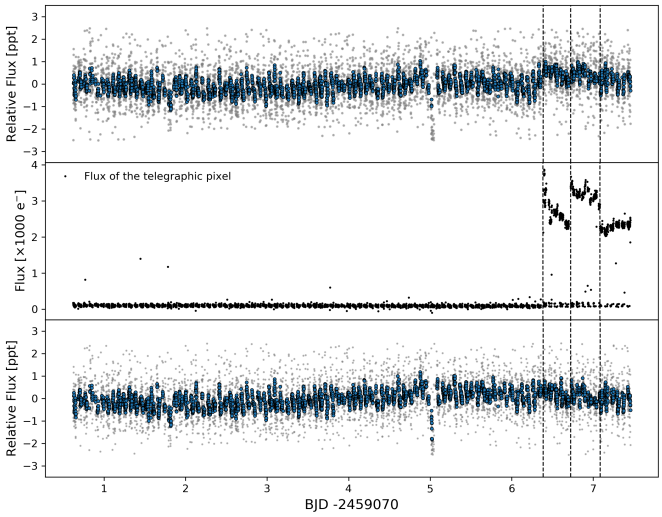

Fig. A.2: TOI-178 normalized light curve of the second visit (gray symbols) with its 10 min smoothed version overplotted (blue symbols) is shown in the top panel. The flux jumps produced by the appearance of a new hot pixel are marked with the dashed vertical lines. The light curve of the detected *telegraphic* pixel is presented in the middle panel showing its anomalous behaviour at the end of the visit. The light curve extracted from the corrected data is shown in the bottom panel. For better visualization, the light curves are presented after a 3-σ clipping and corrected by a second order polynomial in time.

Appendix B: Analysis of the radial velocity data

Appendix B.1: Method

In this appendix, we describe the analysis of the RV data alone. To search for planet detections, we computed the ℓ_1 periodogram of the RV, as defined in Hara et al. (2017). This tool is based on a sparse recovery technique called the basis pursuit algorithm (Chen et al. 1998). It aims at finding a representation of the RV time series as a sum of a small number of sinusoids whose frequencies are in the input grid.

The ℓ_1 periodogram presents the advantage, over a regular periodogram, to search for several periodic components at the same time, and therefore drastically reduces the impact of aliasing (Hara et al. 2017).

The ℓ_1 periodogram has three inputs: a frequency grid, onto which the signal will be decomposed in the Fourier domain, a noise model in the form of a covariance matrix, and a base model. The base model represents offsets, trends, or activity models, and can be understood as follows. The principle behind the ℓ_1 periodogram is to consider the signal in the Fourier domain, to minimise the sum of the absolute value of the Fourier coefficients on a discretized frequency grid (their ℓ_1 norm), while ensuring that the inverse Fourier transform is close enough to the model in a certain, precise sense. Due to the ℓ_1 norm penalty, frequencies "compete" against each other to have non zero coefficients. However, one might assume that certain frequencies, and more largely certain signals are by default in the data, and should not be penalized by the ℓ_1 norm. We can define a linear model whose column vectors are not penalized, which we call the base model.

The signals found to be statistically significant might vary depending on the frequency grid, base and noise models. To explore this aspect, as in Hara et al. (2020), we compute the ℓ_1-periodogram of the data with different assumptions on the noise covariance. The covariance models are then ranked via cross-validation. That is, we fix a frequency grid. Secondly, for every choice of base and noise models, we record which detections are announced. We assess the score of the detections + noise models by cross validation. The data is separated in a training and test set containing respectively 70 and 30 % of the data, chosen at random. The model is fitted onto the training set and one computes the likelihood of the data on the test set. This operation is repeated 250 times, and we attribute the median of the 250 scores to the triplet base model, covariance model and signal detected. To determine if a signal at a given period is significant, we study the distribution of its FAP among the highest ranked models.

Appendix B.2: Definition of the alternative models

To define the alternative RV models, as a preliminary step, we analyse the $H\alpha$, FWHM, bisector span and $\log R'_{HK}$ time-series as provided by the ESPRESSO pipeline. We compute the residual periodograms, as described in (Baluev 2008). These periodograms allow to take into account general linear base models that are fitted along candidate frequencies. We compute the periodgrams and iteratively add a sinusoidal function whose frequency is corresponding the maximum peak of the periodogram. Iterations 1 and 2 are shown in Fig. B.1, respectively top and bottom. We mark with the dotted black the position of 36 days and 16 days (top and bottom, respectively). Pursuing the iterations, we find signals detection with FAP $<10^{-3}$ of periods at 36, 115 and 15.9 for $H\alpha$, 35.5, 20.8 and 145 for the FWHM, 36 and 16 for the bisector span and 36.7 and 16.5 days for the $\log R'_{HK}$. 36 days periodicity always are detected with FAP $< 10^{-6}$. These results indicate that activity effects in the RV at ≈ 36 and ≈ 16 days are to be expected, as well as low frequency effects. These signals likely stem from the rotation period the star, creating signal at the fundamental frequency and the first harmonic.

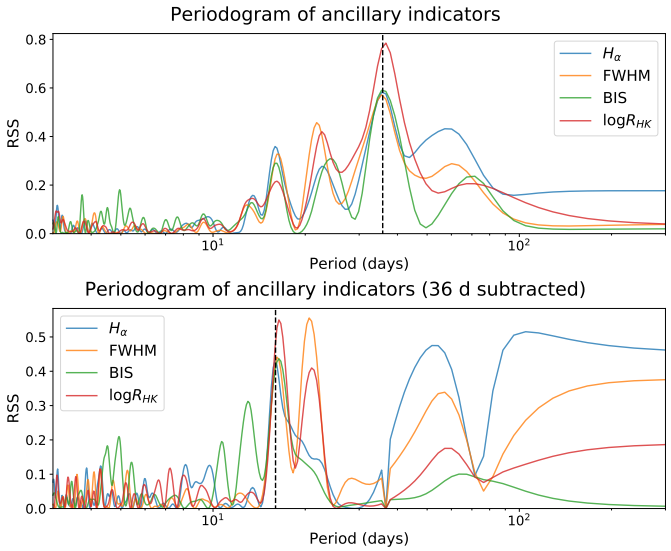

Fig. B.1: Top: periodograms of the raw ancillary indicators time-series ($H\alpha$, FWHM, bisector span and $\log R'_{HK}$. We compute, respectively in blue, orange, green and red). Periodogram of the same timeseries when the signal corresponding to the maximmum peak is injected in the base model.

We now turn to the RV, and define the alternative noise models we explore. These are Gaussian, with a white component, as well as an exponential decay and a quasi-periodic term, as given by the formula

$$V_{kl} = \delta_{k,l}(\sigma_k^2 + \sigma_W^2) + \sigma_R^2 \, \mathrm{e}^{-\frac{(t_k - t_l)^2}{2\tau_R^2}} + \sigma_{QP}^2 \, \mathrm{e}^{-\frac{(t_k - t_l)^2}{\tau_{QP}^2} \sin^2\left(\frac{t_k - t_l}{P_{\rm act}}\right)}. \quad \text{(B.1)}$$

where V_{kl} is the element of the covariance matrix at row k and column l, $\delta_{k,l}$ is the Kronecker symbol, σ_k is the nominal uncertainty on the measurement k, and $\sigma_W, \sigma_R, \tau_R, \sigma_{QP}, P_{\rm act}$ are the parameters of our noise model. A preliminary analysis on the ancillary indicators (FWHM, S-index, $H\alpha$) showed that they all exhibit statistically significant variations at ≈ 40 (36 days), as well as a periodogram peak at 16 d. The 36 and 16 d signals exhibit phases compatible with one another at 1 sigma, except for the 36 d signal in the FWHM which is 3σ away from the phase fitted on the S-index and $H\alpha$. This points to a stellar rotation period of 36 d. We consider all the possible combinations of values for σ_R and σ_W in 0.0,0.5 1.0,1.25, 1.5,1.75,2 m/s, τ = 0, 2, 4, 6 d, $P_{\rm act}$ = 36.5 d, σ_{QP} = 0,1,2,3,4 m/s and τ_{QP} = 18, 36 or 72 d.

The computation of the ℓ_1 periodogram is made assuming a certain base model. By this, we mean a linear model which is assumed to be by default in the data, and thus will automatically be fitted. This base model might represent for instance offsets, trends, or certain periodic signals. We try the following base models: one offset, one offset and smoothed $H\alpha$, one offset and smoothed FWHM, or one offset and the smoothed $H\alpha$ and FWHM time-series. The smoothing of a given indicator is done via a Gaussian process. This process has a Gaussian kernel, whose parameters (time-scale and amplitude) have been optimized to maximise the likelihood of the data.

Appendix B.3: Results

In Fig. B.2, we represent the ℓ_1 periodogram obtained with the noise model with maximum cross validation score with three different base models (from top to bottom: without any indicator, with smoothed $H\alpha$ and with both smoothed $H\alpha$ and smoothed FWHM). In all cases, we find signals at 35-40 d, 15 d and 3.24 d, as well as a peak at 6.55 d. We might also find peaks at 21 d, 9.84 d, 2.08 d, 1.92 1.44, or 1.21 days, depending on the models used. Note that 2.08 and 1.92 d are aliases of each other, so that the presence of one or the other might originate from the same signal. The model with the overall highest cross validation score includes only the smoothed $H\alpha$ time-series in the base model, and with the notations of eq. (B.1), $\sigma_W = 1.75$ m/s, $\sigma_R = 1.5$ m/s, $\tau = 2$ days, $\sigma_{QP} = 0$, and corresponds to the middle figure in Fig. B.2.

We computed the ℓ_1-periodogram on a grid from 0 to 0.95 cycles per day (we then do not consider periods below one day) with all combinations of the base and noise models. As in Hara et al. (2020), the models are ranked with cross validation. We then considered the 20% highest ranked models (all noise and base models considered), which we denote by CV_{20}, and computed the number of times a signal is included in the model. By that, a peak has a frequency within $1/T_{obs}$ of a reference frequency $1/P_0$, where T_{obs} is the observation time-span, and has a FAP below 0.5. We report these values in Table B.1 for the reference periods P_0 corresponding to signals appearing at least once in Fig. B.2. Note that, due to the short time-span, the frequency resolution is not good enough to distinguish 36 and 45 days.

We find that signals at 36, 16 and 3.2 days are consistently included in the model. The 3.2 days signal presents a median FAP of 0.002, and can therefore be confidently detected. When the base model consists only in an offset, 36 and 16 days are systematically significant with FAP <5%, but their significance decreases as activity indicators are included in the model. Since these periodicities appear also in ancillary indicators, we conclude that they are due to activity. Signals at 6.5 and 9.9 days appear in $\approx 15\%$ of the models, but with low significance.

We re-compute the ℓ_1 periodogram by assuming that 3.2, 6.5, 15.9 and 36.7 days are by default in the data, as well as the smoothed $H\alpha$. Furthermore, the detection of a 6.5 d transit signal is clear in TESS data only. Both for the 3.2 and 6.4 signals, we use the phase predicted from the transits for these two planets. This step is done as it improves the ability if the ℓ_1 periodogram to find the smallest amplitude signals. We find of signals at 2.08 d (alias of 1.91 d), 1.21, 16 d and 9.9 days (see Fig. B.3, top). These are only hints, as the false alarm probabilities of these peaks is above 50%. We note that, depending on the frequency grid chosen, a 5.6 d periodicity, alias of 1.21 d, might appear, as shown in Fig. B.3, bottom. Although detections cannot be claimed from the RV data only, we note that there are signals at 2.08 d (alias of 1.91 d) and 9.9 d. We find that they are in phase with the photometric signals within 1.5 σ, which further strengthens the detection of transiting planets at these periods.

When adding in the base model all known transiting planets, as well as the smoothed $H\alpha$ indicators and sine functions at 15.7 and 36 days, we obtain B.4, where a signal at 15.2 days appears with a FAP of $\approx 20\%$.

Table B.1: Inclusion in the 20% best models of different periodicities. We report the false alarm probability (FAP) associated with the best model, the frequency of inclusion in the model and the median FAP in the 20% best models.

Period (d)	FAP (best fit)	Inclusion in the model	CV_{20} median FAP
1.21	$5.33\cdot10^{-1}$	1.730%	-
1.44	1.00	0.0%	-
1.914	1.00	0.0%	-
2.08	$2.93\cdot10^{-1}$	0.384%	-
3.24	$1.33\cdot10^{-2}$	100.0%	$2.20\cdot10^{-3}$
6.5	$1.31\cdot10^{-1}$	15.57%	-
9.9	$3.41\cdot10^{-1}$	16.63%	-
15.2	$8.38\cdot10^{-2}$	89.32%	$6.83\cdot10^{-2}$
20.7	1.00	0.0%	-
36 (45)	$5.24\cdot10^{-1}$	95.48%	$2.57\cdot10^{-1}$

The 20.7 day transiting planet could correspond to the peak at 21.6 d in the ℓ_1 periodogram (Fig. B.2, top). When restricting the frequency grid to 0 to 0.55 cycles per day, the best CV model yields Fig. 7, where a signal at 20.6 days appear. However, signals close to 20.7 days seems to disappear when changing the stellar activity model. The planetary signature might be hidden in the RV due to stellar effect. Further observations would allow to better disentangle stellar and planetary signals.

Appendix B.4: Detections: conclusion

In conclusion, we can claim an independent detection of the 3.2 d planet with RV. We find significant signatures at 36 and 15-16 days, which we attribute to activity. We find signals at 1.91 d or its alias 2.08 d, 6.5 and 9.9 d in phase with the detected transits. We see a signal at 21 d for some models which could correspond to the 20.7 d planet, but it seems that there are not enough points to disentangle a planetary and an activity signals and this period. We finally note that modelling an activity signal at 15.7 days leaves a signal at 15.2 days, which likely stems from the presence of a planet at this period.

Finally, we check the consistency in phase of the signals fitted onto the photometric and RV data. We perform a MCMC computation of the orbital elements on the RVs with exactly the same priors as model 2, except that we set a flat prior on the phases. We find that the uncertainties on the phase corresponding to planets b,c,d,e,f,g correspond respectively to 7, 2, 3,3, 4 and 100% of the period. The phases from transits are included respectively in the 1.5, 1, 2, 1, 1 σ intervals derived from the RVs, such that we deem the phases derived from RVs consistent with the transits.

Appendix B.5: Mass and density estimates

The RV measurements allow to obtain mass estimates of the planets. These ones can depend on the model of stellar activity used. To account for this, we estimate masses with two different stellar activity models: (1) Activity is modelled as two sinusoidal signals plus a correlated noise (2) activity is modelled as a correlated Gaussian noise with a semi-periodic kernel. In both cases, we add the $H\alpha$ time-

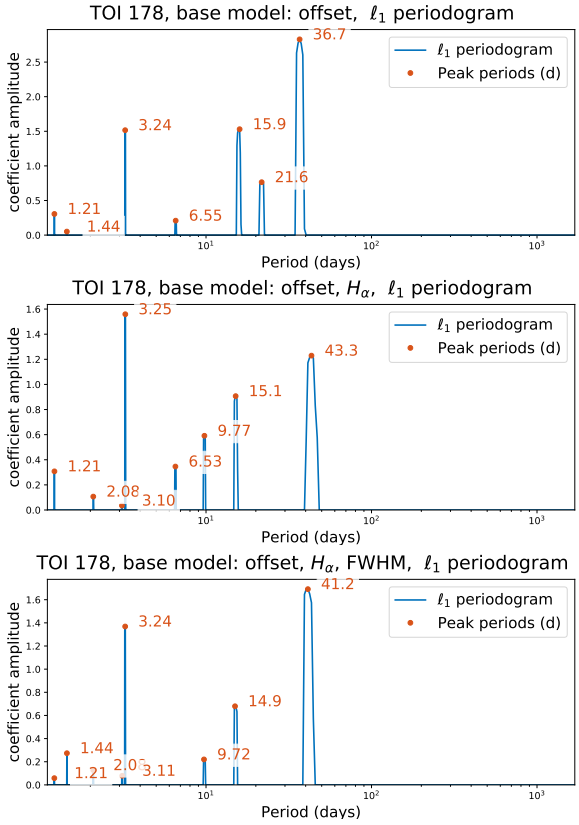

Fig. B.2: ℓ_1 periodogram of the ESPRESSO RV corresponding to the best cross validation score with different linear base models for the data: Top: only one offset, middle: offset, smoothed $H\alpha$, bottom: smoothed $H\alpha$ and smoothed FWHM.

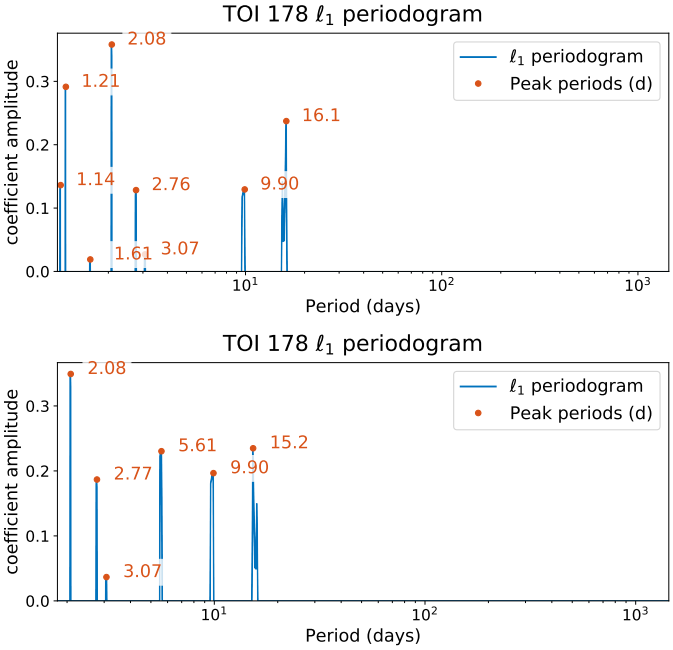

Fig. B.3: ℓ_1 periodogram of the ESPRESSO RV periodogram corresponding to the best cross validation score with a base model including $H\alpha$, the 6.5 d and 3.2 d planets, a 36 and 15.2 d signals. Top: frequency grid from 0 to 0.9 cycles per day, bottom frequency grid from 0 to 0.55 cycles per day.

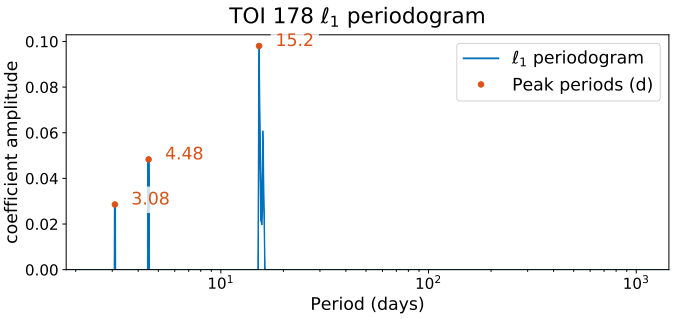

Fig. B.4: ℓ_1 periodogram when all transiting planets are added to the base models, as well as a smoothed $H\alpha$ indicator and sinusoids at 15.7 and 36 days.

series smootheed with a Gaussian process, as described in B.3. In model (1), the two sinusoids have periods of ≈ 40 days and ≈ 16 days. This is motivated by the fact that these periodicities appeared systematically in ancillary indicators, though with different phases. We therefore allow the phase to vary freely in the RVs. The priors on the stellar activity periods are taken as Gaussians with mean 16 days, $\sigma = 1$ day and mean 36.8 days, $\sigma = 8$ days, according to the variability of the position of the peaks appearing in the spectroscopic ancillary indicators. We further add free noise components, a white component and correlated component with an exponential kernel. The prior on the variance is a truncated Gaussian with $\sigma = 16\ m^2/s^2$, the prior on the noise time scale is log-uniform between 1h and 30 days. The second model is a Gaussian process (or here, correlated Gaussian noise), with a quasi-periodic kernel k of the form

$$k(t; \sigma_W, \sigma_R, \lambda, \nu) = \sigma_W^2 + \sigma_R^2\, \mathrm{e}^{-\frac{t}{\tau}} \cos(\nu t). \quad \text{(B.2)}$$

We impose a Gaussian truncated prior on σ_W^2, σ_R^2 with $\sigma = 100\ m^2/s^2$. We impose a flat prior on ν between $2\pi/50$ and $2\pi/30$ rad/day and a log-uniform prior on τ on 1h to 1000 days. For planets b, c, d, g, e, f, the priors on period and time of conjunction are set according to the constraints obtained from the joint fit of TESS and CHEOPS data.

We run an adaptive Monte-Carlo Markov chain algorithm as described in Delisle et al. (2018) implementing spleaf (Delisle et al. 2020), which offers optimized routines to compute the inverse of covariance matrices. We check the convergence of the algorithm by ascertaining that 600 effective samples have been obtained for each variable (Delisle et al. 2018). The posterior medians as well as the 1 σ credible intervals are reported in Table B.2 for both activity models. The kernel (B.2) is close to the Stochastic harmonic oscillator (SHO), as defined in Foreman-Mackey et al. (2017b). We also tried the SHO kernel, and simply imposed that the quality factor Q be greater than one half, the other parameters having a flat priors. We find very similar results, so that they are not reported in Table B.2.

Modelling errors might leave a trace in the residuals. In Hara et al. (2019), it is show that, if the model used for the analysis is correct, the residuals of the maximum likelihood model appropriately weighted should follow a normal distribution and not exhibit correlations. In Fig. B.5, we show the histogram of the residuals (in blue) and a the

Table B.2: mass estimation with activity model as two sinusoids, $H\alpha$ model and correlated noise

Parameter	Estimates (1)	Estimates (2)
Planets		
TOI 178b (1.9 days)		
K [m/s]	$1.07^{+0.17}_{-0.15}$	$1.04^{+0.27}_{-0.28}$
m [$M_\oplus$]	$1.54^{+0.28}_{-0.25}$	$1.49^{+0.40}_{-0.43}$
ρ [$\rho_\oplus$]	$0.93^{+0.20}_{-0.25}$	$0.90^{+0.28}_{-0.31}$
TOI 178c (3.2 days)		
K [m/s]	$2.82^{+0.17}_{-0.17}$	$2.72^{+0.27}_{-0.28}$
$m[M_\oplus]$	$4.85^{+0.46}_{-0.50}$	$4.67^{+0.62}_{-0.58}$
ρ [$\rho_\oplus$]	$0.92^{+0.15}_{-0.19}$	$0.89^{+0.17}_{-0.19}$
TOI 178d (6.5 days)		
K [m/s]	$1.43^{+0.22}_{-0.22}$	$1.24^{+0.33}_{-0.29}$
$m[M_\oplus]$	$3.11^{+0.52}_{-0.57}$	$2.70^{+0.71}_{-0.71}$
ρ [$\rho_\oplus$]	$0.16^{+0.03}_{-0.03}$	$0.14^{+0.04}_{-0.04}$
TOI 178e (9.9 days)		
K [m/s]	$1.52^{+0.25}_{-0.24}$	$1.72^{+0.31}_{-0.35}$
$m[M_\oplus]$	$3.79^{+0.67}_{-0.70}$	$4.28^{+0.82}_{-0.96}$
ρ [$\rho_\oplus$]	$0.37^{+0.07}_{-0.08}$	$0.42^{+0.09}_{-0.10}$
TOI 178f (15.2 days)		
K [m/s]	$2.65^{+0.34}_{-0.30}$	$2.88^{+0.34}_{-0.37}$
$m[M_\oplus]$	$7.60^{+1.05}_{-1.18}$	$8.28^{+1.11}_{-1.34}$
ρ [$\rho_\oplus$]	$0.56^{+0.09}_{-0.10}$	$0.61^{+0.11}_{-0.11}$
TOI 178g (20.7 days)		
K [m/s]	$1.41^{+0.27}_{-0.28}$	$1.19^{+0.42}_{-0.47}$
m [$M_\oplus$]	$4.51^{+0.90}_{-1.00}$	$3.78^{+1.47}_{-1.45}$
ρ [$\rho_\oplus$]	$0.21^{+0.04}_{-0.04}$	$0.17^{+0.06}_{-0.07}$
Other signals)		
Signal at $\approx$ 40 days (probably $P_{\rm rot}$)		
P [days]	$39.4^{+1.09}_{-3}$	-
K [m/s]	$3.01^{+0.35}_{-0.36}$	-
Activity signal at 16 days		
P [days]	$16.2^{+0.28}_{-0}$	-
K [m/s]	$1.07^{+0.44}_{-0.40}$	-
Noise parameters		
σ_W [m/s]	$0.62^{+0.19}_{-0.21}$	$0.90^{+0.26}_{-0.25}$
σ_R [m/s]	$0.47^{+0.18}_{-0.23}$	-
τ_R [days]	$5.74^{+4.03}_{-5.12}$	-
σ_{QP} [m/s]	-	$2.90^{+0.99}_{-1.47}$
τ_{QP} [days]	-	350^{+192}_{-337}
P [days]	-	$42.7^{+3.27}_{-3.72}$

probability distribution function of a normal variable. The two appear to be in agreement. We further compute the Shapiro-Wilk normality test (Shapiro & Wilk 1965) and find a p-value of 0.78, which is compatible with normality. The variogram does not exhibit signs of correlations. The same analysis is performed with model 2, for which the residuals also do not exhibit non normality nor correlation (p value of 0.99 on the rediduals). We conclude that both models are compatible with the data.

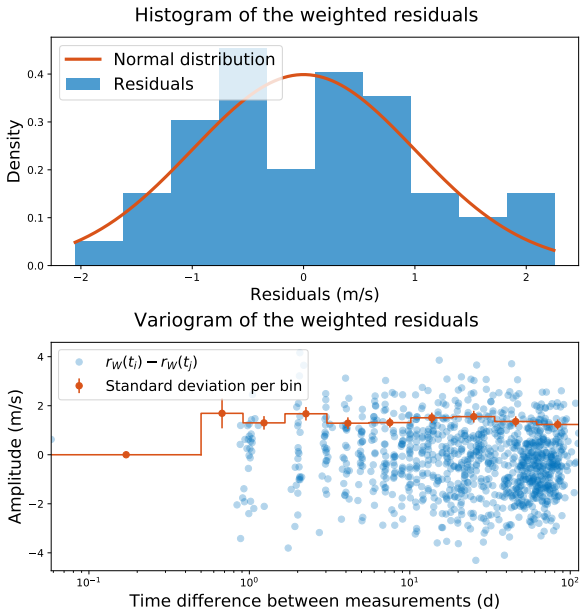

Fig. B.5: Histograms of the weighted residuals of the maximum likelihood model (Top) and their variogram (bottom) for activity modelled as two sinusoidal functions (model 1).

Appendix C: Continuation of a Laplace resonant chain

TOI-178 is in a configuration where successive pair of planet is at the same distance to the exact neighbouring first order MMR. Generalising a bit the configuration, we define fictive planets 1, 2 and 3, such that planets 1 and 2 are close to the resonance $(k_1+q_1):k_1$ and planets 2 and 3 are close to the resonance $(k_2+q_2):k_2$, where the k_i and q_i are integers. we hence write the near-resonant angles:

$$\begin{aligned}\varphi_1 &= k_1\lambda_1 - (k_1+q_1)\lambda_2\,,\\ \varphi_2 &= k_2\lambda_2 - (k_2+q_2)\lambda_3\,,\end{aligned} \tag{C.1}$$

where λ_i is the mean longitude of planet i. The associated distances to the resonances read:

$$\begin{aligned}\Delta_1 &= k_1 n_1 - (k_1+q_1)n_2\,,\\ \Delta_2 &= k_2 n_2 - (k_2+q_2)n_3\,,\end{aligned} \tag{C.2}$$

where n_i is the mean motion of planet i. A Laplace relation exists between these three planets if:

$$j_1\Delta_1 - j_2\Delta_2 \approx 0\,, \tag{C.3}$$

where j_1 and j_2 are integers. In addition, the invariance by rotation of the Laplace angle (D'Alembert relation) gives:

$$j_1 q_1 = j_2 q_2\,. \tag{C.4}$$

As the result, the Laplace relation requires:

$$n_3 \approx \frac{k_2 n_2 - \frac{q_2}{q_1}\Delta_1}{k_2+q_2}\,, \tag{C.5}$$

which translates as, for the period of the 3rd planet:

$$P_3 \approx \frac{k_2+q_2}{\frac{k_2}{P_2} - \frac{q_2}{q_1 P_{1,2}}}\,, \tag{C.6}$$

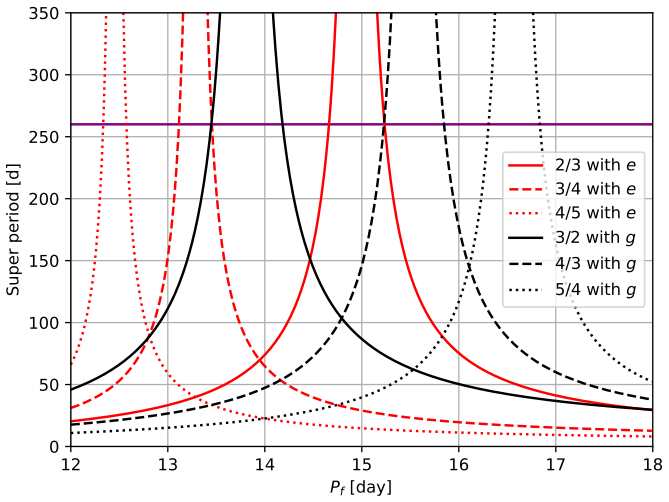

Fig. C.1: Super-period of planet f with respect to e (in red) and g (in black) for a set of first order MMR. The purple line indicate the value of the super-period between the other pairs of the chain 260 day. Only two possible period allowed planet f to be part of the resonant chain, which correspond to the near-intersection of the right-hand side of a red curve, left-hand side of a black curve, and the purple horizontal line.

where $P_{1,2}$ is the super-period associated to Δ_1. From this we can compute the periods of potential additional planets that would continue the Laplace resonant chain of TOI-178. Taking planets e and f as planets 1 and 2, the formula to compute the possible period of a planet x that could continue the resonant chain becomes:

$$P_x = \frac{k+q}{\frac{k}{P_f} - \frac{q}{P_{f,g}}}, \tag{C.7}$$

where $P_{f,g}$ is the super-period between the near first-order resonances of the known chain defined by eq. (1), here $\sim$ 260 days. and k and q are integers such that planet x and f are near a $(k+q)/k$ MMR. Some of the relevant periods are displayed in table 7.

Similar computation allowed us to determine the possible period of planet f before its confirmation by CHEOPS, see Fig. C.1

Appendix D: Internal structure

We provide here the posterior distributions of the planetary interior models, as well as some more details on their calculations.

As mentioned in the main text, deriving the posterior distribution of the internal structure parameters requires computing millions of times the radius of planets for different set of parameters. In order to speed up this calculation, we have first computed a large (five millions points) database of internal structure models, varying the different parameters. This database was split randomly in three sets, one training set (80% of models), one validation set and one test set (each of them containing 10 % of the whole database). We have then in a second time fitted a Deep Neural Network in order to be able to compute very rapidly the

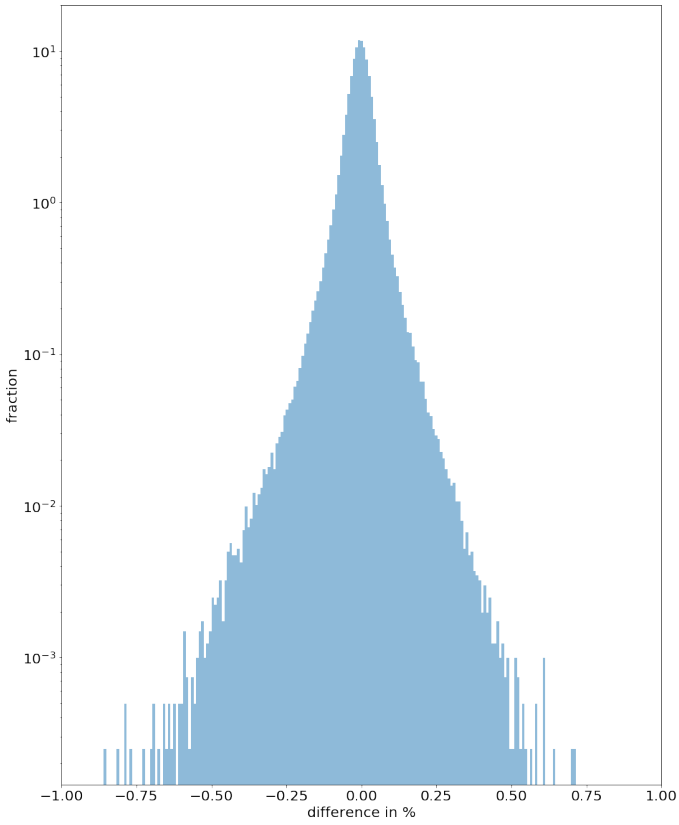

Fig. D.1: Histogram of prediction error from our DNN on the test set. The y axis is in log scale, and the x axis covers an error from -1% to 1%.

radius of a planet with a given set of internal structure parameters. The architecture of the DNN we used is made of 6 layers of 2048 nodes each, and we used the classical ReLU as activation function (Alibert & Venturini 2019). The DNN is trained for a few hundreds epochs, using a learning rate that is progressively reduced from $1.e-2$ down to $1.e-4$. Our DNN allows to compute these radii with an error below 0.25% on average with a speed up of many orders of magnitude (a few thousands models computed per second). Fig. D.1 shows the prediction error we reach on the test set (which was not used for training). The error on the predicted radius is lower than 0.4%, an error much smaller than the uncertainty on the radii we obtained for the TOI-178 planets, in 99.9% of the cases. It is finally important to note that this model does not include the compression effect that would be generated by the gas envelope onto the solid part. Given the mass of the gas envelop in all planets, this approximation is justified.

The following plots shows the posterior distribution of the interior structure parameters. The parameters are the inner core, mantle and water mass fraction relative to the mass of the solid planet, the Fe, Si, Mg molar fraction in the mantle, the Fe molar fraction in the core, and the mass of gas (log scale). It is important to remember that since the core, mantle and water mass fractions add up to one, they are not independent. This is also the case for the Si, Mg and Fe molar fraction in the mantle.

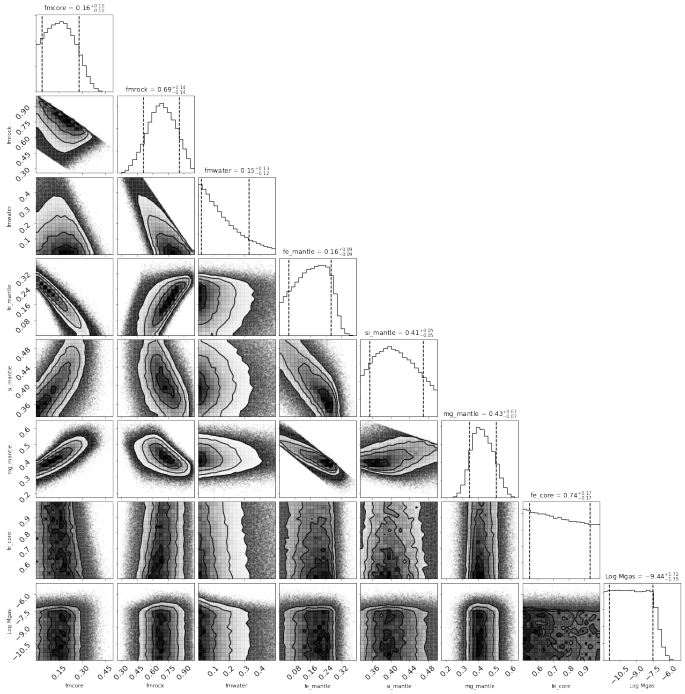

Fig. D.2: Corner plot showing the main parameters of the internal structure of planet b. The parameters are the core mass fraction, mantle mass fraction, water mass fraction (all relative to the solid planet), molar fractions of Fe, Si and Mg in the mantle, molar fraction of Fe in the core, and mass of gas (log scale). The dashed lines give the positions of the 16% and 84% quantiles, the number on top of each column give the median and the same quantiles.

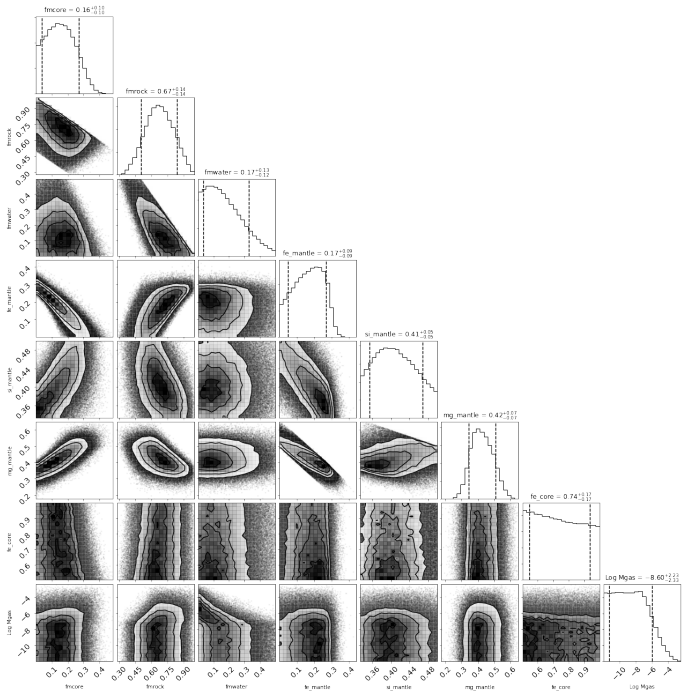

Fig. D.3: Same as Fig. D.2 for planet c.

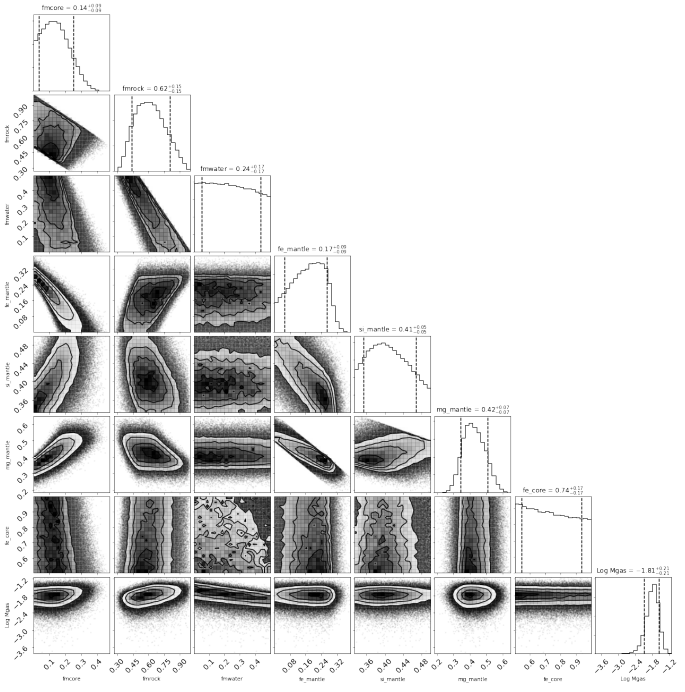

Fig. D.4: Same as Fig. D.2 for planet d.

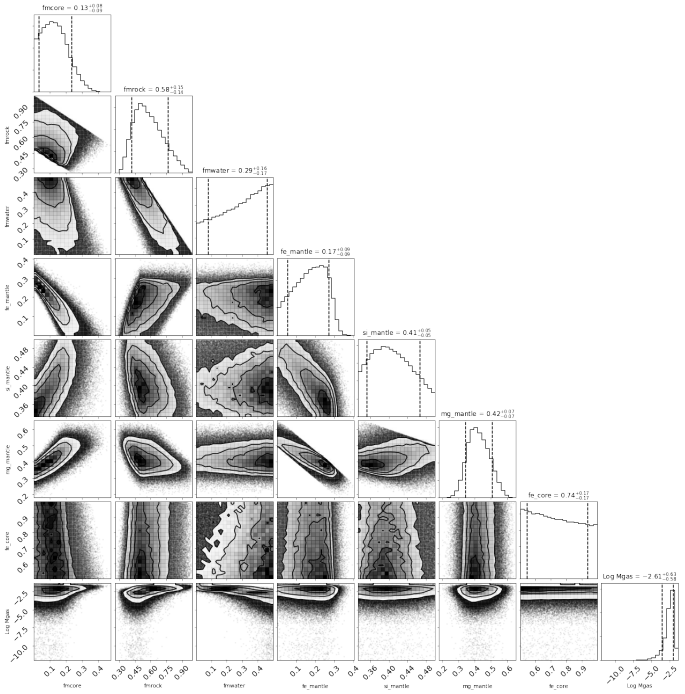

Fig. D.5: Same as Fig. D.2 for planet e.

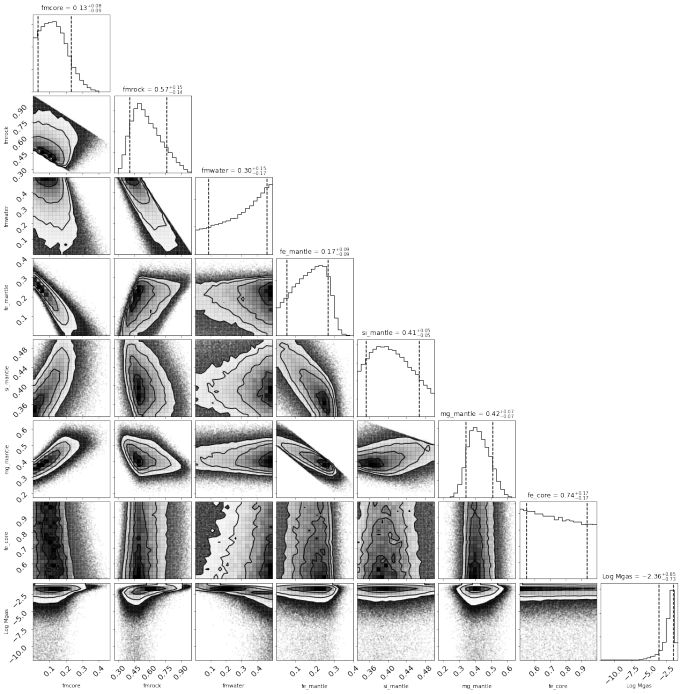

Fig. D.6: Same as Fig. D.2 for planet f.

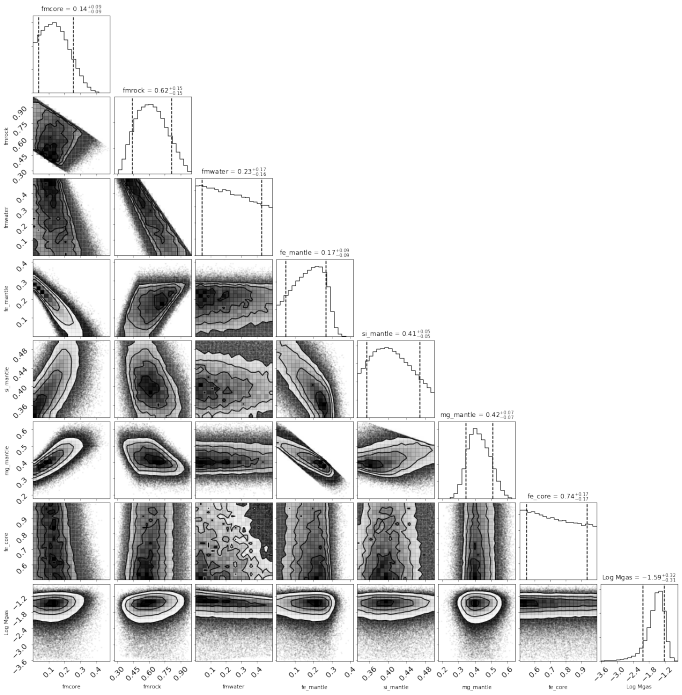

Fig. D.7: Same as Fig. D.2 for planet g.